JOURNAL OF THERMOPHYSICS AND HEAT TRANSFER
Vol. 40, No. 1, January–March 2026

Performance Impact of Coolant Oxidation on Transpiration Cooling for Sharp Hypersonic Vehicles

Anthony Mannion,* Danny Ko,† Yongho Sungtaek Ju,‡ and Xiaolin Zhong§
University of California Los Angeles, Los Angeles, California 90095

https://doi.org/10.2514/1.T7150

A main limiting design consideration for hypersonic flight vehicles is surface heating. State-of-the-art thermal protection systems (TPS), such as ablative heat shields, are limited in that they require blunt geometries and often experience surface degradation through material removal. Evaporative transpiration TPS can protect sharp leading edges without experiencing surface degradation. A study is conducted investigating the effect of coolant oxidation on the performance of evaporative transpiration TPS. The study uses three-dimensional direct numerical simulation algorithms considering thermochemical nonequilibrium flow around a 3.1 mm nose tip radius flying at Mach 15 and an altitude of 30 km. Aluminum is chosen as the coolant because of its high latent heat of vaporization and low molar mass. The exothermic oxidation reactions are shown to greatly increase the incident heat flux and require over twice the coolant mass flux at the stagnation point to maintain a leading-edge temperature near the saturation temperature of the coolant. This effect is prevalent even under the nonequilibrium conditions of very slow reaction speeds, 10^{-11} times lower than their accepted values. Therefore, oxidation reactions cannot be neglected. Understanding how coolant oxidation impacts the performance of evaporative transpiration TPS helps to inform future design of evaporative transpiration TPS.

Nomenclature

$C_{f,c}$	=	reaction rate coefficient
c_s	=	mass fraction of species, s
c_p	=	specific heat, J/(kg · K)
D	=	binary or mixture diffusion coefficient, m^2/s
e	=	specific energy, J/kg
e_{ext}	=	extrapolated relative error
F_j	=	inviscid flux vector
G_j	=	viscous flux vector
GCI_{fine}	=	fine-grid convergence index
h	=	specific enthalpy, J/kg
h_s°	=	species heat of formation, J/kg
HTC	=	heat transfer coefficient, $\text{MW}/(\text{m}^2 \cdot \text{K})$
K_{eq}	=	equilibrium constant, mol/m^3
K_c	=	chemical equilibrium ratio
k	=	thermal conductivity, $\text{W}/(\text{m} \cdot \text{K})$
$k_{f,c}$ and $k_{b,c}$	=	forward and backward reaction rates
L	=	latent heat of vaporization, J/mol
M	=	molar mass, kg/mol
$\dot{m}$	=	mass flux, $\text{kg}/(\text{m}^2 \cdot \text{s})$
MTC	=	mass transfer coefficient, m/s
P	=	pressure, Pa
q	=	heat flux, $\text{W}/(\text{m}^2 \cdot \text{K})$
Q_{T-v_s}	=	vibrational energy exchange
R	=	universal gas constant, $\text{J}/(\text{mol} \cdot \text{K})$
R_C	=	reaction rate
S	=	standoff distance of the shock, m
T	=	temperature, K
U	=	conserved flow variable vector
u_n	=	velocity in nth direction, m/s
W	=	source vector
α	=	accommodation coefficient
$\delta_{i,j}$	=	Kronecker delta
ϵ	=	emissivity
θ	=	nondimensional temperature
μ	=	viscosity, Pa·s
ν	=	species diffusion velocity, m/s
ρ	=	density, kg/m^3
σ	=	Stefan–Boltzmann constant, 5.670×10^{-8} $\text{W}/(\text{m}^2 \cdot \text{K}^4)$
τ	=	chemical timescale ratio
$\tau_{i,j}$	=	viscous stress, Pa
ω	=	rate of species production, $\text{kg}/(\text{m}^3 \cdot \text{s})$

Subscripts

0	=	stagnation quantity
1	=	one grid point upstream of the stagnation point
c	=	reaction number
eq	=	equilibrium or saturation
i, j	=	grid point location
(l)	=	liquid state
ns	=	total number of species
p	=	product
r	=	reactant
s	=	species number
T	=	translational-rotational
v	=	vibrational
w	=	wall conditions

Presented as Paper 2024-4029 at the 2024 AIAA Aviation Forum, Las Vegas, NV, July 29–August 2, 2024; received 11 October 2024; accepted for publication 25 May 2025; published online 29 August 2025.

*Ph.D. Candidate, Mechanical and Aerospace Engineering Department; ajmannion@g.ucla.edu.
†Ph.D. Graduate, Mechanical and Aerospace Engineering Department.
‡Professor, Mechanical and Aerospace Engineering Department.
§Professor, Mechanical and Aerospace Engineering Department. Associate Fellow AIAA.

I. Introduction

DESPITE increasing interest in hypersonic flight systems, their practical use remains limited. One of the main challenges presented by hypersonic flight systems is the severe incident heat loads present during atmospheric hypersonic flight. These extreme heat loads arise due to compressive heating behind the bow shock. Smaller leading-edge radii, which offer higher lift-to-drag ratios, exacerbate the high incident heat fluxes experienced during hypersonic flight because a linear reduction in leading-edge radius leads to a linear increase in the squared incident heat flux [1,2].

Thermal protection systems (TPS) are used to protect hypersonic vehicles from these high incident heat loads. Current state-of-the-art TPS include ablative heat shields such as those used on the Apollo reentry capsules and passive insulating tiles such as those used on the Space Shuttle. Ablative heat shields, often made of carbon, are

effective at counteracting large incident heat fluxes and can withstand heat fluxes over 30 MW/m^2 [3]. But because ablative heat shields rely on vaporization of their surface material to absorb the incident heat flux, they undergo significant shape change during use [3,4]. Blunt shapes must be used with ablative TPS as surface degradation prevents them from maintaining sharp geometry. Surface degradation also prevents ablative TPS from being reusable. Passive insulating tiles are not as capable of counteracting large incident heat fluxes as ablative heat shields and still require a blunt leading edge to decrease the severity of the incident heat flux.

In addition, postshock conditions give rise to such extreme temperatures that there is significant dissociation of air molecules. For example, diatomic oxygen dissociates at 2000 K [5], well below the postshock temperature for atmospheric hypersonic flight. This creates a highly reactive flow environment as air molecules dissociate, recombine, and react with the leading-edge surface. Even passive insulating tiles are not completely reusable, as exposure to these highly reactive conditions degrades the tiles over time.

It is therefore desirable to develop TPS capable of providing adequate thermal protection while mitigating the limitations of current TPS. Evaporative transpiration TPS are promising in addressing these limitations. Evaporative transpiration TPS continuously supply a sacrificial liquid coolant to the leading-edge surface where the coolant is vaporized. The vaporization of the liquid coolant absorbs the incident heat load during flight in a process similar to ablation. Distinct from an ablative TPS, the expended liquid coolant from an evaporative transpiration TPS can be continually replenished through a porous leading edge. The liquid-vapor coolant layer thereby physically shields the leading edge from high external temperatures and highly chemically reactive flows. In this way, evaporative transpiration TPS do not experience vaporization of the leading-edge structural material itself nor surface degradation along the leading edge. As such, evaporative transpiration TPS eliminate both the requirement for blunt shapes and the single-use limitation of current ablative TPS. The prospective use of sharp leading-edge geometry, owing to evaporative transpiration TPS, could greatly increase the lift-to-drag ratios and maneuverability of hypersonic flight systems. Current studies have shown that evaporative transpiration TPS are as effective as ablative TPS at counteracting incident heat fluxes. Ko et al. [6] have shown that, provided a sufficient coolant mass flux, evaporative transpiration TPS can counteract heat fluxes as high as 85 MW/m^2 along a 3.1 mm nose tip radius leading edge at Mach 20 and 30 km altitude. A diagram showing the operation of an evaporative transpiration TPS is presented in Fig. 1.

Evaporative transpiration TPS function through the vaporization of liquid coolant along a porous leading-edge surface, often made from carbon, silica, or refractory metals. The coolant is stored in an internal reservoir, and solid coolant particles may need to be melted inside this reservoir and pumped toward the porous leading edge. The coolant is then drawn through the porous material to the surface by external pressure and capillary action. Once the liquid coolant reaches the surface, it absorbs the incident heat flux and vaporizes, discharging into the hypersonic flow as vapor.

Many previous studies have investigated using gases as the transpiration coolant material [7–16]. Van Forest et al. [17] and Huang et al. [11] investigated using liquid water as the transpiration coolant material, and Ko et al. [6] investigated using metals and oxides as the transpiration coolant material. Luo et al. [18] showed that liquid coolants are substantially more effective than gaseous coolants, as they undergo a phase change along the leading-edge surface. As a result, it is desirable to use liquid coolants in transpiration TPS to utilize the energy absorption of evaporation.

Van Foreest et al. [17] conducted experiments using liquid water as the coolant for an evaporative transpiration TPS. This experiment saw a leading edge exposed to a heat flux of 2.8 MW/m^2. The leading edge was cooled to less than 300 K, the saturation temperature of water, using a mass flow rate of only 0.2 g/s of water. Many transpiration TPS required an external pumping system to supply the liquid coolant, making them unfeasible for practical use. Huang et al. [11] developed a transpiration TPS that utilized capillary action to draw coolant from an internal reservoir, as shown in Fig. 1. Liquid water was used as the coolant and was drawn through a hydrophilic porous medium that facilitated the capillary action. As with Forest et al. [17], the surface temperature was maintained at approximately 373 K. The manageable heat flux of 1.1 MW/m^2 was limited mainly by the self-pumping capability of the porus media. While the work of Van Foreest et al. and Huang et al. [11,17] demonstrated the effectiveness of evaporative transpiration TPS, much larger heat fluxes must be counteracted during atmospheric hypersonic flight.

Metallic and oxide coolants are capable of counteracting these large incident heat fluxes using reasonable coolant mass fluxes due to their high latent heats of vaporization. Metals and oxides also have a wide range of material properties, offering greater flexibility in material selection under a wide range of flight environments and material limits of the leading-edge surface. Weston [8] showed that performance of transpiration TPS using cold gasses are influenced by the material properties of the coolant, namely heat capacity and molar mass. Ko et al. [6] showed that the molar mass, the latent heat of phase change, and the saturation temperature are critical to the performance of evaporative transpiration TPS.

Additionally, near the stagnation point along sharp leading edges, mass diffusion is large due to coolant vaporization. The mass diffusion rate may even be larger than the evaporative mass transfer rate, as predicted by Scala and Vidale [19] and Charwat [20] using kinetic theory. Many previous numerical studies have assumed that the leading-edge surface is in a state of thermodynamic equilibrium, but this assumption is invalid if the mass diffusion rate is larger than the evaporative mass transfer rate at the leading-edge surface.

Kubota and Baker [21,22] have shown that assuming thermodynamic equilibrium along a vaporizing leading-edge surface can result in erroneously low predictions for the leading-edge temperature due to the large mass diffusion rates common with transpiration TPS. Underpredicting the surface temperature of an evaporative transpiration TPS can lead to surface temperatures large enough to melt the leading-edge material or cause vapor bubbles to nucleate within the porous media. Nucleation of vapor bubbles within the porous media is a mode of TPS failure referred to as surface dry-out, and has been observed by Faghri while studying heat pipes and He and Wang while studying transpiration TPS [23,24]. Avoiding underpredicting the leading-edge temperature motivates the use of thermochemical nonequilibrium flow solvers when studying evaporative transpiration TPS, as in the work of Ko et al. [6] and when studying ablative TPS as in [25–28].

A recent investigation by Ko et al. [6] studied evaporative transpiration TPS, allowing for thermochemical nonequilibrium, through a parametric study on coolant material properties, flight conditions, and nose tip radii. The parametric study was conducted using a model

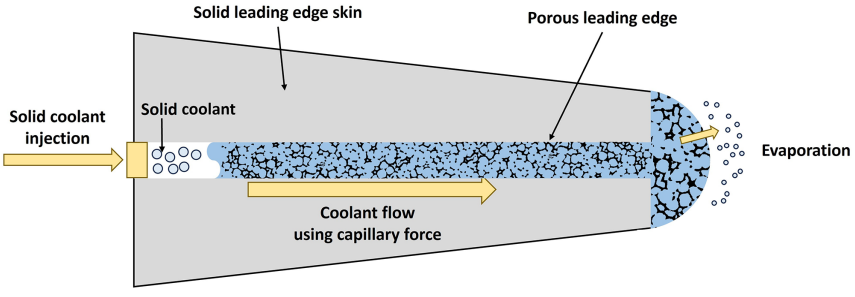

Fig. 1 Example diagram showing how an evaporative transpiration TPS functions [6].

based on the boundary-layer theory presented by Scala and Vidale [19]. This model makes use of many simplifying assumptions and were valid only along the stagnation line, so additional solutions were obtained using DNS algorithms to augment the parametric study. It was found that evaporative transpiration TPS using metallic and oxide coolants could withstand heat fluxes up to 85 MW/m^2, though larger heat fluxes could theoretically be cooled by increasing coolant mass flux. Ko et al. [6] also determined that oxides are chemically inert when used as the coolant for evaporative transpiration TPS because of their chemically stable nature and the significant presence of oxygen in the flowfield, which limits oxide dissociation. Coolant oxidation was neglected in the study by Ko et al. [6].

This study aims to examine the effects of oxidation of metallic coolants on the performance of evaporative transpiration TPS. Metals oxidize readily at elevated temperatures, and the presence of oxygen in the flow promotes, rather than inhibits, chemical reactions with metallic species. Oxidation reactions are exothermic, and the prevalence of these reactions may increase the incident surface heat flux. Additionally, coolant oxidation is expected to draw the evaporated coolant away from the leading-edge surface as it reacts with incoming oxygen. This effect would increase the required coolant mass flux. Therefore, it is important to understand the physical impact of oxidation reactions on the external flowfield and how they affect the performance of evaporative transpiration TPS using metallic coolants.

Through studies conducted using DNS algorithms, the effects of coolant oxidation reactions on the surface heating and the required coolant mass flux of evaporative transpiration TPS are evaluated. The simulations are conducted only within the laminar region of the leading-edge surface. In order to characterize a broader range of coolant oxidation reactions, the reaction rate coefficient was varied through the range of feasible speeds for oxidation reactions. The results of this study bring evaporative transpiration TPS a step closer to future implementation.

II. Governing Equations and Material Properties

To accurately detail the effects of metallic coolant oxidation in evaporative transpiration TPS, it is preferred to fully solve the complete Naiver–Stokes equations without using simplified models. This is because viscous effects are influential when considering boundary-layer phenomena. The boundary layer is of great importance to the study of evaporative transpiration TPS, as the transpiration process occurs almost entirely inside the boundary layer, as shown by Scala and Vidale [19]. Additionally, heat and mass transfer phenomena are responsible for the diffusion of coolant species, for the vaporization of coolant material, and for the heat fluxes present along the leading edge of evaporative transpiration TPS. Heat and mass transfer phenomena are confined deep within the boundary layer of evaporative transpiration TPS, further motivating a complete solution of the full Naiver–Stokes equations. Since the performance of transpiration TPS is heavily dependent on boundary-layer phenomena, heat and mass transfer phenomena, and the surface conditions along the leading edge, DNS algorithms are preferred over simplified models. Simulations using DNS algorithms are therefore used to directly simulate the influence of mass diffusivity, viscosity, and thermal conductivity of the gas phase mixture in the complete Naiver–Stokes equations without any simplifying modeling of the flow.

In addition, chemical reactions are extremely important for both atmospheric hypersonic flight, which exhibits substantial dissociation of air species, and evaporative transpiration TPS using metallic coolants, which may involve chemically reactive coolants. As such, a thermochemical nonequilibrium solver is preferred to accurately simulate the time-dependent effects of chemical reactions and vibrational energy exchange, which may occur on a similar timescale as the flow speed.

Aluminum is considered as the metallic coolant for this study. Aluminum has a molar mass of 27 g/mol and a latent heat of vaporization of 319 kJ/mol. The saturation temperature of aluminum at standard temperature and pressure is 2750 K. Due to aluminum's low molar mass and high latent heat of vaporization, it is expected that large incident heat fluxes could be counteracted with low coolant mass fluxes of aluminum, as shown by Ko et al. [6]. In addition, oxidation reactions of aluminum are relatively well-documented, allowing for more accurate solutions of the relevant chemical reactions. This is important because it is currently unknown whether the oxidation reactions will behave as though they are in a frozen state, a nonequilibrium state, or an equilibrium state. At the flow temperatures present in these solutions, aluminum is expected to oxidize readily with the supply of oxygen provided by the freestream.

Therefore, three-dimensional steady-state simulations are conducted using DNS algorithms for an evaporative transpiration TPS with an aluminum coolant. These simulations consider the complete solution of the Naiver–Stokes equations for a reacting flow in thermochemical nonequilibrium. The simulations are conducted within the laminar region of the leading-edge surface. An altitude of 30 km and a Mach number of 15 are chosen as the flight condition for this study. This flight condition aligns with the center of the parametric study on flight conditions conducted by Ko et al. [6] and represents the highest Mach number along the lowest altitude curve for typical flight trajectories of hypersonic vehicles from Anderson [5]. Low altitude flight conditions are desirable for this study because higher density flows at low altitudes require larger coolant mass fluxes [6]. This allows the effects of exothermic oxidation reactions to be studied under the most demanding flight conditions. The nose radius considered in this study is 3.1 mm, once again matching the study of Ko et al. [6]. The DNS algorithms consider the Naiver–Stokes equations formulated for 7 species (N_2, O_2, NO, AlO, N, O, Al). Thermochemical nonequilibrium is accounted for using a two-temperature model to represent translational-rotational energy and vibrational energy. The conservative three-dimensional Navier–Stokes equations are then formulated for a total of 7-species conservation equations, 3 momentum conservation equations in the x, y, and z directions, the total energy conservation equation, and the vibrational energy conservation equation. The governing equations can be expressed in vector form as

$$\frac{\partial U}{\partial t} + \frac{\partial F_j}{\partial x_j} + \frac{\partial G_j}{\partial x_j} = W \tag{1}$$

In Eq. (1), U represents the state vector of conserved quantities, F_j represents the inviscid flux vector, G_j represents the viscous flux vector, and W represents the source terms of each conserved quantity as

$$U = \begin{bmatrix} \rho_1 \\ \cdots \\ \rho_{\text{ns}} \\ \rho u_1 \\ \rho u_2 \\ \rho u_3 \\ \rho e \\ \rho e_v \end{bmatrix} \quad W = \begin{bmatrix} \omega_1 \\ \cdots \\ \omega_{\text{ns}} \\ 0 \\ 0 \\ 0 \\ 0 \\ \sum_{s=1}^{nms} (Q_{T-v_s} + \omega_s e_{v,s}) \end{bmatrix}$$

$$F_j = \begin{bmatrix} \rho_1 u_j \\ \cdots \\ \rho_{\text{ns}} u_j \\ \rho u_1 u_j + p\delta_{1j} \\ \rho u_2 u_j + p\delta_{2j} \\ \rho u_3 u_j + p\delta_{3j} \\ (p + \rho e) u_j \\ \rho e_v u_j \end{bmatrix} \quad G_j = \begin{bmatrix} \rho_1 v_{1j} \\ \cdots \\ \rho_{\text{ns}} v_{\text{ns}j} \\ -\tau_{1j} \\ -\tau_{2j} \\ -\tau_{3j} \\ -u_i \tau ij - k_T \dfrac{\partial T}{\partial x_j} - k_v \dfrac{\partial T_v}{\partial x_j} \\ + \sum_{s=1}^{nms} \rho_s h_s v_{sj} \\ -k_v \dfrac{\partial T_v}{\partial x_j} + \sum_{s=1}^{nms} \rho_s h_s v_{sj} \end{bmatrix}$$

The diffusion velocity of each species, v_{sj}, is defined using Fick's law of diffusion:

$$u_{sj} = U_j + v_{sj} \tag{2a}$$

$$v_{sj} = -\frac{D_s}{c_s}\frac{\partial c_s}{\partial x_j} \tag{2b}$$

where u_{sj} is the velocity of each species in the j-direction and D_s is the diffusivity of each species. The viscous stress τ_{ij} is computed as

$$\tau_{ij} = \mu\left(\frac{\partial u_i}{\partial x_j} - \frac{\partial u_j}{\partial x_i}\right) + \frac{2\mu}{3}\left(\frac{\partial u_k}{\partial x_k}\right)\delta_{ij} \tag{3}$$

The viscous flux term G_j can be seen to be heavily influenced by both viscous effects and diffusion of each species as governed by mass transport phenomena.

Blottner's relationship [29] is used to determine the viscosity and thermal conductivity of air and aluminum. The coefficients from Blottner et al. [29] and Gupta et al. [30] are used for the air species. The evaporating species transport properties are estimated using kinetic theory from Hirschfelder et al. [31]. The kinetic diameter of aluminum vapor is estimated using a curve fit based on data presented by Breck [32]. Wilke's semi-empirical relationship [33] is then used to calculate the viscosity and thermal conductivity of the mixture. Finally, to determine the mixture diffusivity, a constant Schmidt number of 0.5 is assumed, as in [34]. A Schmidt number of 0.5 is representative of flows where all species have a similar molar mass [34]. The Schmidt number is defined as

$$Sc = \frac{\mu}{\rho D} = 0.5 \tag{4}$$

A. Thermochemical Nonequilibrium

The reactions contributing to dissociation and recombination of each species are

$$N_2 + M \longrightarrow 2N + M \tag{R1}$$

$$O_2 + M \longrightarrow 2O + M \tag{R2}$$

$$NO + M \longrightarrow N + O + M \tag{R3}$$

$$AlO + M \longrightarrow Al + O + M \tag{R4}$$

$$N_2 + O \longrightarrow NO + N \tag{R5}$$

$$NO + O \longrightarrow N + O_2 \tag{R6}$$

$$N_2 + O_2 \longrightarrow 2NO \tag{R7}$$

Reactions (R1–R4) are dissociation reactions, and reactions (R5–R7) are exchange reactions. The reaction rates R_c for the dissociation reactions are

$$R_c = \sum_{s=1}^{NS}\left(-\boldsymbol{k}_{f,c,s}\frac{\rho_{r_1}}{M_{r_1}}\frac{\rho_s}{M_s} + \boldsymbol{k}_{b,c,s}\frac{\rho_{p_1}}{M_{p_1}}\frac{\rho_{p_2}}{M_{p_2}}\frac{\rho_s}{M_s}\right) \tag{5}$$

The reaction rates for the exchange reactions are

$$R_c = -\boldsymbol{k}_{f,c}\frac{\rho_{r_1}}{M_{r_1}}\frac{\rho_{r_2}}{M_{r_2}} + \boldsymbol{k}_{b,c}\frac{\rho_{p_1}}{M_{p_1}}\frac{\rho_{p_2}}{M_{p_2}} \tag{6}$$

The forward and backward components of each reaction, $k_{f,c}$ and $k_{b,c}$, are

$$\boldsymbol{k}_{f,c} = C_{f,c}T_a^{\eta_c}\exp(-\theta_d/T_a) \tag{7}$$

$$\boldsymbol{k}_{b,c} = \boldsymbol{k}_{f,c}/K_{\text{eq}} \tag{8}$$

The forward reaction rates are computed from [35–39]. The equilibrium constants calculated based on curve fits made from Park [36], McBride et al. [40], and NIST-JANAF tables [41].

The vibrational energy per unit volume is

$$\rho e_v = \sum_{s=1}^{\text{NDS}}\rho_s e_{v,s} = \sum_{s=1}^{\text{NDS}}\rho_s\left(\sum_{m=1}^{\text{NMOD}}\frac{g_{s,m}R}{M_s}\frac{\theta_{v,s,m}}{\exp(\theta_{v,s,m}/T_v) - 1}\right) \tag{9}$$

where $g_{s,m}$ is the degeneracy of each vibrational mode. NDS and NMOD refer to the number of molecular species and the number of vibrational modes of each species, respectively. The characteristic vibrational temperatures and their degeneracies are taken from [36]. The vibrational characteristics of aluminum oxide are approximated as those of silicon oxide from Johnston [38] due to lack of data on aluminum oxide. The two species are assumed to have similar vibrational characteristics due to the similar molecular weights of the materials and the similarity between the bond of AlO and SiO. To determine the source term in the vibrational energy, the Landau–Teller expression is used:

$$Q_{T-v,s} = \rho_s\frac{e_{v,s}(T) - e_{v,s}(T_v)}{\langle\tau_s\rangle + \tau_{cs}} \tag{10}$$

Additionally, two dimensionless parameters are used to analyze the prevalence of chemical nonequilibrium in the results. Both parameters are evaluated along the stagnation line. The first dimensionless parameter used is the chemical equilibrium ratio, K_c, which describes the relationship between the equilibrium condition for species concentration at a location in the flow and the actual species concentrations at that location. The dissociation reaction (R4) is considered when determining the chemical equilibrium ratio:

$$K_c = \frac{P_{\text{Al}}P_{\text{O}}}{P_{\text{AlO}}K_{\text{eq},c}} \tag{11}$$

Where P_s represents the partial pressure of a given species and K_{eq} represents the equilibrium constant for reaction c. A chemical equilibrium ratio of one shows that the species concentrations agree with the values predicted by the equilibrium constant. A value greater than one suggests that reaction (R4) has not reached completion and that there is excess concentration of aluminum and/or oxygen. A value less than one shows the reverse case. The equilibrium ratio may deviate from one due to other reasons, however, such as with fuel-rich or fuel-lean reaction environments in combustion systems.

The second dimensionless parameter used is the chemical timescale ratio τ, defined as the ratio of the chemical timescale to the flow speed:

$$\tau = \frac{\omega_{\text{AlO}} * S}{\rho_0 u_0} \tag{12}$$

where ω represents the species source term and is evaluated at each point along the stagnation line, while the density and flow speed ρ and u are taken at the stagnation point to better reflect the mass flux of the vaporized aluminum coolant. S is a characteristic length scale, taken in this case as the standoff distance of the shock. This means that the chemical timescale ratio represents the ratio between the rate at which aluminum oxide is forming and the rate at which the mass flux of vaporized coolant would travel along the stagnation line from the stagnation point toward the shock.

In reality, the physical stagnation point is offset from the leading-edge surface. This is due to the finite velocity of the evaporative mass flux of coolant normal to the leading-edge surface. As the flow speed approaches zero, the time constant will approach infinity. This motivates the use of a consistent flow speed parameter in defining the chemical timescale constant.

It is suspected that the reaction location will be centered around the physical stagnation point, along with the maximum concentration of aluminum oxide. The colloquial definition of the stagnation point, being located at the surface, is used throughout the rest of this paper to improve readability despite a nonzero surface velocity. The physical stagnation point is specified when needed.

Finally, the heat transfer coefficient HTC and mass transfer coefficient MTC are evaluated for the external flow as

$$\mathrm{HTC} = \frac{q}{T_w - T_{0,\mathrm{inf}}} \tag{13}$$

$$\mathrm{MTC} = \frac{\dot{m}_s}{\rho_{s,0} - \rho_{s,\mathrm{inf}}} \tag{14}$$

where s is the coolant species, 0 represents the stagnation point, and inf represents freestream values. Note that q represents the incident heat flux into the surface. Heat and mass diffusion into the liquid coolant or solid leading-edge surface is not considered in this study. Therefore, the HTC and MTC are only computed for the external flow.

Typically, the HTC and MTC are calculated considering the wall superheat and the species concentration inside the liquid compared to the temperature and species concentration inside the gas phase. This is because in most heat transfer applications, especially involving phase changes, a hot wall provides the necessary heat flux and nucleation sites for a phase change to occur. Therefore, when determining the HTC, the wall is the source of energy, the liquid is the sink, and the heat flux is the energy flow from the source to the sink. This frames the relationships describing the HTC and MTC as being analogous to Ohm's law, where the HTC and MTC are the inverse of the resistance values.

In the case of coolant vaporization along a hypersonic leading edge, the incoming gas flow is responsible for providing the necessary heat flux for the liquid coolant to vaporize. Therefore, for the HTC in Eq. (14), the source of energy is the freestream flow, the liquid coolant is the sink, and the incident heat flux is the transfer of energy between the two. For the MTC, the source of coolant species is the surface concentration of gaseous coolant as in the work of Scala and Vidale [19], the sink is the freestream concentration of gaseous coolant, and the coolant mass flux is the transfer of gaseous coolant between the two. This motivates the definition of the HTC and MTC in this paper. Note that the value of $\rho_{s,\mathrm{inf}}$ is zero, as there is no coolant naturally in the freestream. The equations for the HTC and MTC are similar to those of Li and Nagamatsu [42] and Nagamatsu et al. [43]; however, temperature has been used here instead of enthalpy in order to keep the HTC and MTC dimensional as in other phase change research such as in the works of Li and Nagamatsu [42] and Nagamatsu et al. [43].

Additionally, the freestream stagnation temperature is expected to be much larger than the wall temperature. This is because the wall temperature is lowered by all cumulative thermodynamic effects along the stagnation line such as energy absorption by the vibrational energy mode, dissociation of molecular species, and the cooling flux provided by the TPS itself. Because the temperature difference between the freestream stagnation temperature and the surface temperature is expected to be very large, the HTC is expected to be much lower for evaporative transpiration TPS than with other phase change phenomena.

B. Numerical Model

A high-order accuracy shock-fitting algorithm developed by [34,44] is used for spatial-discretization. The coordinate system undergoes a transformation from the Cartesian coordinate system (x, y, z, t) to the shock-fitted coordinate system (ξ, η, ζ, τ) parallel, normal, and tangential to the leading-edge surface.

$$\begin{bmatrix} \frac{\partial}{\partial x} \\ \frac{\partial}{\partial y} \\ \frac{\partial}{\partial z} \\ \frac{\partial}{\partial t} \end{bmatrix} = \begin{bmatrix} \xi_x & \eta_x & \zeta_x & 0 \\ \xi_y & \eta_y & \zeta_y & 0 \\ \xi_z & \eta_z & \zeta_z & 0 \\ 0 & \eta_t & 0 & 1 \end{bmatrix} \begin{bmatrix} \frac{\partial}{\partial \xi} \\ \frac{\partial}{\partial \eta} \\ \frac{\partial}{\partial \zeta} \\ \frac{\partial}{\partial \tau} \end{bmatrix} \text{ and}$$

$$\begin{bmatrix} \frac{\partial}{\partial \xi} \\ \frac{\partial}{\partial \eta} \\ \frac{\partial}{\partial \zeta} \\ \frac{\partial}{\partial \tau} \end{bmatrix} = \begin{bmatrix} x_\xi & y_\xi & z_\xi & 0 \\ x_\eta & y_\eta & z_\eta & 0 \\ x_\zeta & y_\zeta & z_\zeta & 0 \\ x_\tau & y_\tau & z_\tau & 1 \end{bmatrix} \begin{bmatrix} \frac{\partial}{\partial x} \\ \frac{\partial}{\partial y} \\ \frac{\partial}{\partial z} \\ \frac{\partial}{\partial t} \end{bmatrix} \tag{15}$$

The Naiver–Stokes equations in the transformed coordinates are rewritten as

$$\frac{1}{J}\frac{\partial U}{\partial \tau} + \frac{\partial E'}{\partial \xi} + \frac{\partial F'}{\partial \eta} + \frac{\partial G'}{\partial \zeta} + \frac{\partial E'_v}{\partial \xi} + \frac{\partial F'_v}{\partial \eta} + \frac{\partial G'_v}{\partial \zeta} + U\frac{\partial (1/J)}{\partial \tau} = \frac{W}{J} \tag{16}$$

with

$$E' = \frac{F_1\xi_x + F_2\xi_y + F_3\xi_z}{J} \tag{17a}$$

$$F' = \frac{F_1\eta_x + F_2\eta_y + F_3\eta_z}{J} \tag{17b}$$

$$G' = \frac{F_1\zeta_x + F_2\zeta_y + F_3\zeta_z}{J} \tag{17c}$$

$$E'_v = \frac{G_1\xi_x + G_2\xi_y + G_3\xi_z}{J} \tag{17d}$$

$$F'_v = \frac{G_1\eta_x + G_2\eta_y + G_3\eta_z}{J} \tag{17e}$$

$$G'_v = \frac{G_1\zeta_x + G_2\zeta_y + G_3\zeta_z}{J} \tag{17f}$$

A seven-point stencil is then used to discretize the spatial derivatives as

$$\frac{\partial f_i}{\partial x} = \frac{1}{hb_i}\sum_{k=-3}^{3} a_{i+k} f_{i+k} - \frac{\alpha}{6!b_i} h^5 \left(\frac{\partial f^6}{\partial^6 x}\right) \tag{18}$$

with

$$a_{i\pm 3} = \pm 1 + \frac{1}{12}\alpha \tag{19a}$$

$$a_{i\pm 2} = \pm 9 + \frac{1}{2}\alpha \tag{19b}$$

$$a_{i\pm 1} = \pm 45 + \frac{5}{4}\alpha \tag{19c}$$

$$a_i = -\frac{5}{3}\alpha \tag{19d}$$

$$b_i = 60 \tag{19e}$$

where α in this equation is a term representing the artificial dissipation.

For simulations without a reacting coolant, the third-order Runge–Kutta time-stepping algorithm developed by Williamson [45] is used to advance the solution in time. Oxidation reactions occur extremely fast; however, to resolve those reactions, a second-order trapezoidal scheme by Mortensen [34] is used.

C. Boundary Conditions

The wall boundary conditions are obtained by taking the surface mass balance for each chemical species:

$$\dot{m}_s = \rho_s u_n - \rho D_s \frac{\partial c_s}{\partial \eta} \tag{20}$$

and the energy balance at the surface:

$$k_T \frac{\partial T}{\partial \eta} + k_v \frac{\partial T_v}{\partial \eta} + \sum_{s=1}^{Ns} \rho h_s D_s \frac{\partial c_s}{\partial \eta} = \sigma \epsilon T^4 + \dot{m} \sum_{s=1}^{Ns} c_s h_{s,0} \tag{21}$$

where

$$h_{s,0} = \left(c_{v_s} + \frac{R}{M_s} \right) T + e_{v_s} + h_s^\circ + \frac{1}{2}(u_1^2 + u_2^2 + u_3^2) \tag{22}$$

The energy balance considers the conductive heat flux, the mass diffusion heat flux, and the radiative heat flux. The conductive heat flux into the leading-edge surface is considered equal to the energy needed to raise the aluminum to its saturation temperature. Note that k is the thermal conductivity of the mixture, D_s is the diffusivity of each species, c_s is the species mass fraction, h_s is the species enthalpy, $h_{s,0}$ is the stagnation enthalpy of each species, and η is the wall-normal direction.

One of the species mass flux equations is substituted for the equation of state of the gas mixture. The pressure gradient at the surface is nonzero owing to the mass flux of vaporizing coolant. Lagrange polynomials are used to extrapolate pressure toward the surface as in [34]. The primitive flow variables of species density, wall-normal velocity, and temperature are solved for using these boundary conditions.

The surface mass flux $\dot{m}_s$ of the vaporizing coolant is obtained using the Hertz–Knudsen equation:

$$\dot{m}_s = \alpha_s \sqrt{\frac{M}{2\pi R T_w}} (P_{\text{eq}} - P_s) \tag{23}$$

P_s is the partial pressure of the coolant vapor and P_{eq} is the saturation pressure of the coolant vapor at surface conditions; α_s is the accommodation coefficient and represents the probability that a molecular collision will lead to a reaction. For vaporization reactions, the accommodation coefficient for liquids has been shown to be typically equal to one [19]. The saturation pressure at surface conditions is calculated using the Clausius–Clapeyron equation:

$$P_{\text{eq}} = P^* \exp\left[\frac{L}{R} \left(\frac{1}{T^*} - \frac{1}{T_w} \right) \right] \tag{24}$$

P^* and T^* are the saturation pressure and temperature of aluminum under standard conditions.

The surface mass flux, species mass balance, and energy balance equations for the boundary conditions are coupled, and so require an iterative procedure to solve. A second-order Taylor series is used to represent the change in the primitive flow variables between iterations. Newton's iteration method is used to obtain a solution to the boundary conditions. For further details about the solution procedure to these boundary conditions, see [34].

III. Validation of the Models

The DNS algorithms, chemical reactions, boundary conditions, and vaporization process were previously validated for a 5-species air code, a 6-species code with a nonreacting coolant, and an 11-species code with carbon ablation. The validation of the DNS algorithms and the 5-species nonequilibrium code is detailed in [46]. The validation of the 6-sepcies code is detailed in [6]. The validation of the 11-species code is detailed in [34]. The previous validation studies [6,34,46] serve to validate the unchanged portion of the DNS code used in this study.

The previous 6-species code considered a nonreacting coolant. The 6-species simulations with aluminum coolant therefore consider the species of (N_2, O_2, NO, N, O, Al). Changes made to the 6-species code of [6] resulted in a new 7-species code allowing for an additional chemical reaction between the coolant species and atomic oxygen. There are currently no experimental data available to directly validate the new 7-species code. Instead, a comparison case is conducted for the new 7-species code with the reaction rate of the new oxidation reaction set to 0. These results are compared to the previously validated 6-species code considering the same coolant material. The comparison shows proper implementation of all new algorithms in the new code. The comparison is shown in Table 1. Once again, the colloquial definition of the stagnation point, being located at the surface, is used here despite a nonzero surface velocity.

The difference between the 6-species and 7-species solutions for nonreacting coolants is negligible, less than 0.1% for flow variables and surface heat and mass fluxes. The small differences may be attributed to the different time-stepping algorithms used in each code, the iterative procedure used inside the boundary conditions, and the different time convergence history of each solution. These small and explainable differences serve as validation of the 7-species code.

Stagnation line profiles of the mass fraction of aluminum and oxygen for the nonreacting 6- and 7-species solutions are presented in Fig. 2. The x-axis is normalized as a percentage of the standoff distance of the shock, and the solution is plotted on a semilog scale. The left and right bounds of the plotting regions are the postshock and near-surface locations, respectively.

Figure 2 shows that the nonreacting 6- and 7-species solutions are indistinguishable along the entire stagnation line. The reaction rate is then slowly increased in the 7-species code to verify that the new reactions are implemented correctly. The solutions show proper conservation of mass and energy principles. Additionally, the reaction rates are confirmed to vary with temperature as described in established literature [35–41], showing proper implementation of the reaction curve fits. The expected changes in the flow due to the implementation of these chemical reactions are observed, specifically in temperature due to the additional energy released by the exothermic reaction.

Additionally, a grid refinement study is performed considering grid sizes of 30×80, 60×160, 120×320, and 240×640 grid points. The results show that there is at most a 0.33% difference in the stagnation point pressure and a 0.71% difference in the concentration of aluminum at the stagnation point among the different grid sizes studied. The 120×320 grid size is used in this study to

Table 1 Comparison of the stagnation point properties for nonreacting flow solutions

Property	6-species	7-species nonreacting
Pressure, kPa	328.6	328.6
Temperature, K	2646	2647
Density, kg/m^3	0.375	0.375
Mass fraction of Al	0.186	0.186
Coolant mass flux, kg/(m^2 · s)	0.986	0.987
Incident heat flux, MW/m^2	15.05	15.06
Evaporative heat flux, MW/m^2	13.66	13.67
Radiative heat flux, MW/m^2	1.389	1.391

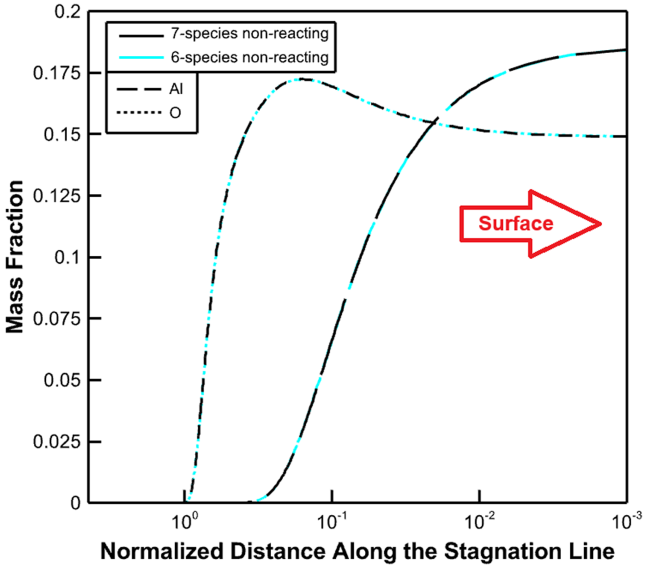

Fig. 2 Normalized stagnation line profiles of the species mass fractions for the nonreacting 6- and 7-species solutions.

obtain high-resolution solutions inside the boundary layer. Additional information about the relative error between the grid sizes used can be found in Table 2, based on the procedures of Celik et al. [47].

Solutions are obtained using Purdue's ANVIL high-performance computing clusters, which consist of compute nodes with 128 cores per socket. The solutions are run from previously converged solutions published in [6], which considered similar coolant materials. This provided an initial guess close to converged results and reduced the computational time needed to reach converged solutions.

Figure 3 shows the stagnation pressure, the saturation pressure of aluminum along the leading-edge surface, and the partial pressure of aluminum along the leading-edge surface. These variables are plotted for both the 7-species reacting coolant solutions and the 6-species nonreacting coolant solutions. The leftmost boundary is the stagnation location, and traveling rightward corresponds to traveling circumferentially along the leading-edge surface. The stagnation quantity is taken at the surface for clarity, despite a finite surface mass flux of coolant.

As can be seen in Fig. 3, the partial pressure of aluminum vapor is lower than the saturation pressure of aluminum along the entire surface. This is consistent with Eq. (23), and coolant flows toward the surface along the entire leading-edge where it is vaporized. If the saturation pressure of aluminum were to drop below the partial pressure of aluminum, then condensation would be expected to occur. The relationship between the different pressures shown in Fig. 3 expresses specific observable trends that match how the flow should be behaving physically. This check serves to validate that the physical relationships governing the coolant mass flux are appropriate. The total surface pressure remains well above the other pressures shown in Fig. 3.

Table 2 Relative error in c_{Al} between grid sizes

Grid	Relative error, %	e_{ext}, %	GCI_{fine}, %
60×160	0.71	1.7	2.1
120×320	0.51	1.2	1.5
240×640	0.09	0.02	0.03

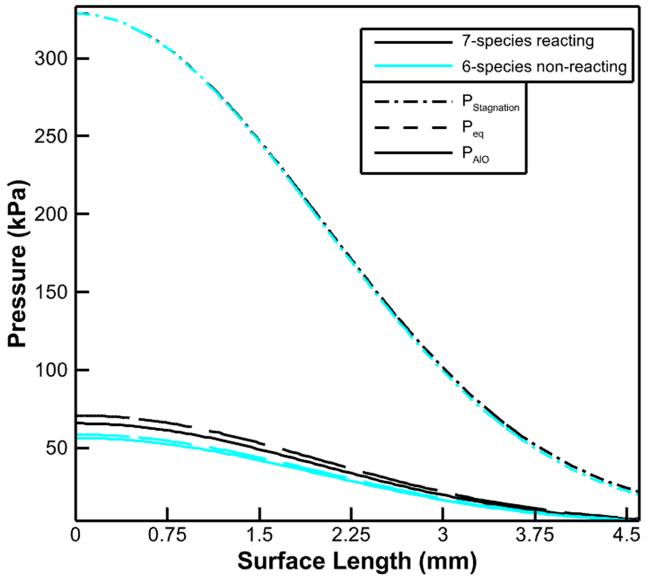

Fig. 3 Surface pressure comparison.

IV. Impact of Coolant Vapor Oxidation

In order to determine the effect of coolant oxidation on the performance of evaporative transpiration TPS, a 7-species study is conducted considering the oxidation of aluminum coolant vapor. Figure 4 shows contour plots of temperature for the 6- and 7-species solutions. The standoff distance of the shock varies

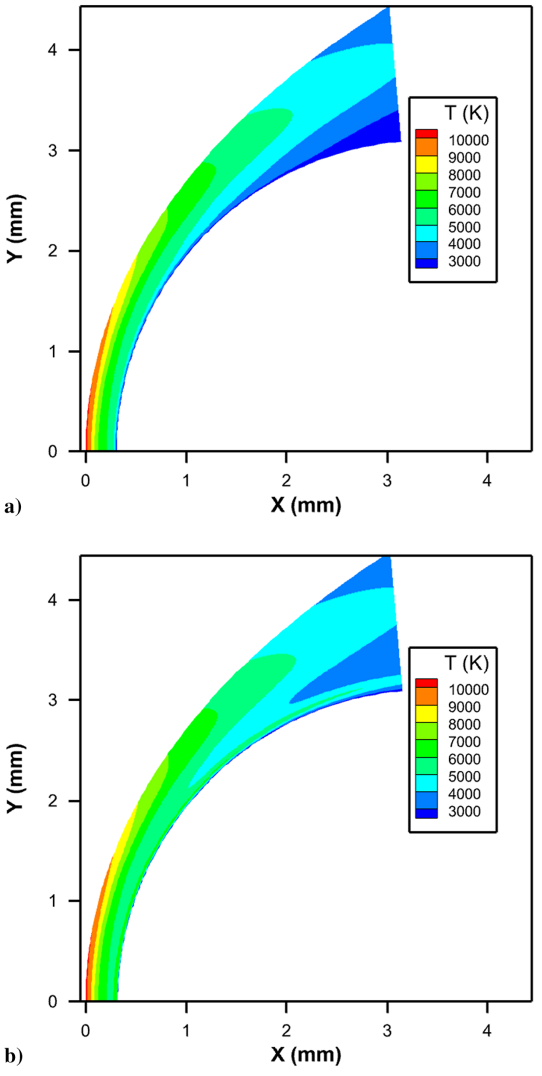

Fig. 4 Contour plots of the temperature for 6-species (top) and 7-species (bottom) solutions.

between different solutions as a result of differences in the flow properties caused by the oxidation reaction. Therefore, in subsequent figures, the x-axis is rescaled to be normalized as a percentage of the standoff distance of the shock. The normalization procedure allows for a more direct comparison between the different solutions. These results are plotted on semilog plots, with the x-axis being in log scale. The semilog plot allows for better comparison of the results near the stagnation point, where the gradients of flow variables become important. The normalized logarithmic x-axis is used in Fig. 5, showing a comparison of the mass fractions of reacting species along the stagnation line between the 6- and 7-species solutions, and Fig. 6, showing a comparison of the temperature and vibrational temperature along the stagnation line between the 6- and 7-species solutions. In these figures, the left and right bounds of the plotting regions are the postshock and near-surface locations, respectively. Because the normalization process leaves the wall grid point at a normalized, distance of zero along the stagnation line, the wall gird point is not shown. All other data points are shown. Once again, the colloquial

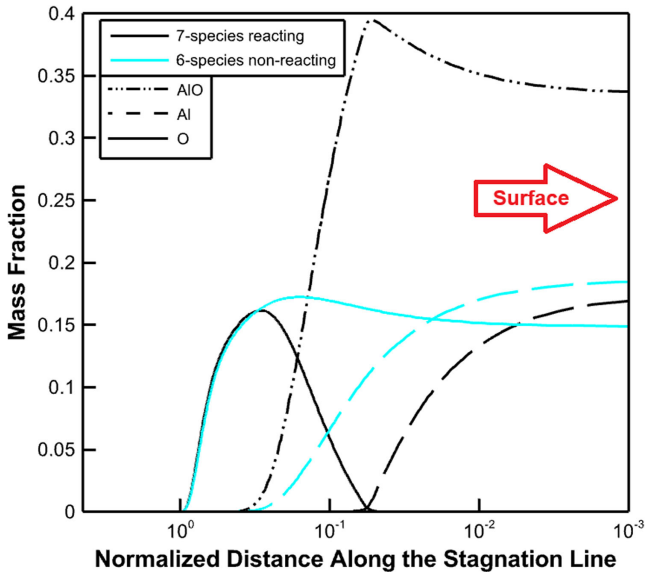

Fig. 5 Normalized stagnation line profiles of the species mass fractions for 6- and 7-species solutions.

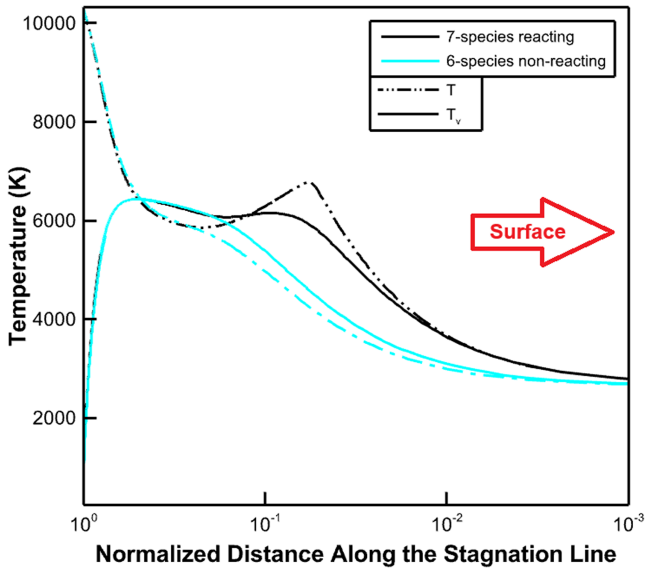

Fig. 6 Normalized stagnation line profiles of the temperature and vibrational temperature for 6- and 7-species solutions.

definition of the stagnation point, being located at the surface, is used here despite a nonzero surface velocity.

The temperature for the 7-species solution in Fig. 4 can be seen to be elevated near the leading-edge surface when compared to the 6-species solution. Figure 6 shows a specific region of elevated temperature in the 7-species solution, which is not present in the 6-species solution. The flow temperature is about 2500 K hotter at this location in the 7-species solution. The peak temperature of this region of elevated temperature occurs at a normalized distance of 0.057 along the stagnation line, or approximately 20 micrometers from the stagnation point in physical length. Figure 5 shows that the location of maximum oxide concentration occurs at 0.053 along the stagnation line. The relative closeness of these regions suggests that the region of elevated temperature is caused by the energy released through the exothermic oxidation reaction of aluminum and the resulting formation of aluminum oxide. Additionally, the thermal conductivity of the gas mixture in the 7-species solution is 11% lower than in the 6-species solution at the stagnation point. Therefore, the increased incident heat flux must be due to a larger temperature gradient and not differing properties of the gas mixtures.

Figure 7 presents contour plots of the mass fractions of aluminum species in the 7-species solution. This figure also shows streamlines as white lines. This plot is zoomed in near the stagnation point to better illustrate the species concentration profiles. The left and right bounds of the contour regions are the postshock and near-surface locations, respectively.

Figures 5 and 7 show the stagnation point mass fraction of aluminum is equal to 0.173 for the 7-species solution, which is 7% lower than the 6-species solution. This result is counterintuitive, as the exothermic oxidation reaction should increase the incident heat flux and lead to an increase in the required coolant mass flux. A larger coolant mass flux should raise the near-surface concentration of coolant. While the oxidation reaction does consume aluminum in the 7-species solution, drawing more aluminum vapor into the flow, there is also a large presence of aluminum oxide at the stagnation point in the 7-species solution. Figures 5 and 7 show a stagnation point mass fraction of 0.34 aluminum oxide. The high mass fraction of the relatively heavy aluminum oxide and the consumption of the additional supply of aluminum to produce this oxide decrease the near-surface concentration of aluminum vapor.

Figure 5 and 7 also show that the location of the maximum concentration of aluminum oxide occurs away from the surface, at the same location where all oxygen and aluminum are consumed in the 7-species solution. This suggests that the reaction occurs instantly at this location, as upstream of this location there is no aluminum present to form aluminum oxide, and downstream of this location there is no oxygen to form aluminum oxide. The changing concentration gradients of the reactant species are due to diffusion of the aluminum oxide product away from the reaction location, lowering the mass fraction of the other species. The streamlines in Fig. 7 illustrate that the physical stagnation point is offset from the leading-edge surface.

Figure 8 shows the bulk velocity of the flow as well as the diffusion velocity, from Eq. (2b), of each reacting species along the stagnation line for the 7-species solution. The distance along the stagnation line has been normalized by the standoff distance of the shock and plotted on a semilog axis. Note that the diffusion velocity is not equivalent to the species velocity. A black horizontal line through 0 m/s has been drawn for easy reference, as well as a red vertical line at the location of the maximum mass fraction of aluminum oxide. Also note that the velocity presented in this figure is the x component of velocity along the stagnation line. As such, velocities pointing downstream of the shock are positive as per the coordinate system seen in Fig. 7.

Figures 7 and 8 show that the bulk velocity is directed away from the stagnation point when near the leading-edge surface, owing to the vaporization of coolant. There is also no oxygen available to react in this region, so no aluminum oxide can form here. The aluminum oxide present near the leading-edge surface is suspected to have been transported from upstream via diffusion. This is confirmed by the diffusion velocity profile in Fig. 8. Figure 8 also

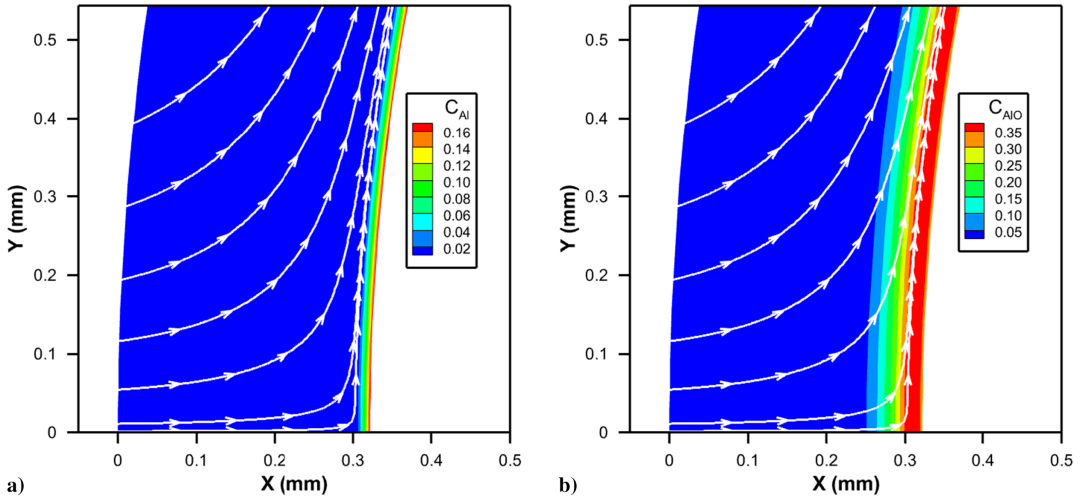

Fig. 7 Contour plots for the 7-species mass fractions of Al (left) and AlO (right).

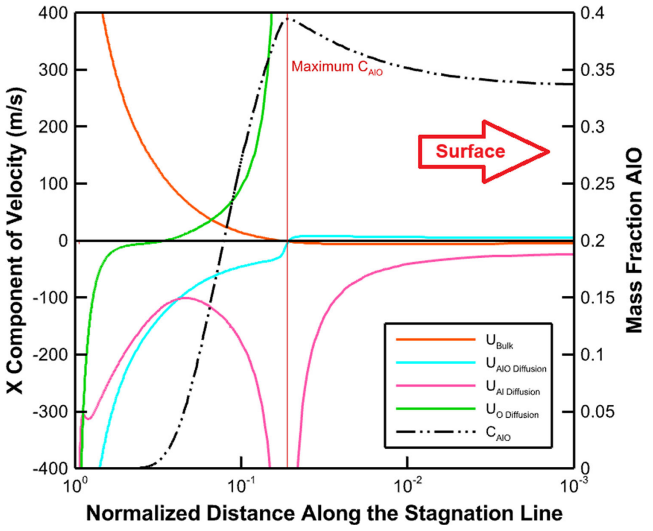

Fig. 8 Bulk and diffusion velocities.

confirms that the results are physical because the diffusion velocity of aluminum oxide is directed away from the location of maximum aluminum oxide concentration.

The diffusion velocity of aluminum oxide is substantial, being comparable to or in excess of the bulk velocity. The diffusion velocity of aluminum downstream of the location of maximum aluminum oxide concentration location is substantially larger than the bulk velocity in the region and directed upstream toward the location of maximum aluminum oxide concentration. The large diffusion velocity of aluminum shows that the diffusive mass flux is larger than the evaporative mass flux, motivating the need for a thermochemical nonequilibrium flow solver as discussed with Scala and Vidale [19] and Charwat [20].

Aluminum's diffusion velocity approaches infinity as all aluminum is consumed. The value for the diffusion velocity of aluminum upstream of the location of maximum aluminum oxide concentration is not physically meaningful, as there is not a significant concentration of aluminum past this location. The diffusion velocity approaches infinity because both the concentration and the concentration gradient in Eq. (2b) driving the diffusion velocity approach infinity. The concentration approaches infinity more rapidly than the concentration gradient does, so the diffusion velocity approaches infinity.

The diffusion velocity of atomic oxygen upstream of the location of maximum aluminum oxide concentration can be seen approaching infinity and moving in the downstream direction. Once again, this is because at the location of maximum aluminum oxide concentration there is not a significant concentration of atomic oxygen, and the diffusion velocity becomes nonphysical. Near the postshock region, the diffusion velocity of all the species plotted approaches infinity as the postshock condition assumes that the flow is composed of only undissociated air, N_2, and O_2. The concentration of all the other species at the postshock location is zero.

Finally, the bulk velocity at the location of maximum aluminum oxide dissociation is zero. This physical stagnation point, where the flow speed is zero, can be seen to be offset from the leading-edge surface as discussed with Eq. (12). As the flow speed approaches zero, the oxidation reaction has effectively an infinite amount of time to proceed, leading to the large formation of aluminum oxide at this location. These observations confirm and explain the species concentration profiles of Figs. 5 and 7. Additionally, these findings solidify the necessity for fully solving the Naiver–Stokes equations to account for mass diffusivity, viscosity, and thermal conductivity due to the prevalence of these phenomena.

Table 3 presents the important flow variables and the surface mass and heat fluxes for the 6- and 7-species solutions at the stagnation point. Additionally, a 6-species solution is shown considering a coolant identical to nonreacting aluminum but with a latent heat of vaporization a factor of 2.5 times less than that of aluminum. A third 6-species solution is shown for a nonreacting coolant with a molar mass that is a factor of 2.6 times greater than that of aluminum. The values of 2.5 and 2.6 are approximate and are chosen to keep the coolant properties as rational values, while achieving a coolant mass flux similar to the reacting 7-species case. These additional solutions are obtained to further evaluate the effect of coolant oxidation on the performance of an evaporative transpiration TPS. A previous study by Ko et al. [6] shows how coolant properties alter evaporative transpiration TPS performance. Using the results from [6], it is determined that the required coolant mass flux of aluminum, when undergoing oxidation, is equivalent to the required coolant mass flux of a nonreacting coolant with the decreased latent heat of vaporization or the increased molar mass. Once again, the colloquial definition of the stagnation point, being located at the surface, is used here despite a nonzero surface velocity.

Table 3 demonstrates that the coolant oxidation reaction raises the stagnation temperature to 2681 K, a 1.3% increase from the nonreacting 6-species solution. An increase in surface temperature is expected due to the increased heating from the exothermic oxidation reaction. However, there is an exponential relationship between the surface temperature and the mass flux as shown by Eqs. (23) and (24). As such, the surface temperature will remain near the saturation temperature of aluminum, as even a small increase in the surface temperature in Eq. (24) greatly raises the evaporate mass flux in Eq. (23). A small mass flux of vaporizing coolant can provide a large evaporative heat flux, and so a small increase in

Table 3 Comparison of the stagnation point flow properties

Property	6-species	7-species reacting	6-species $1/2.5\,h_s^*$	6-species 2.6 M
Pressure, kPa	328.6	328.6	328.6	328.6
Temperature, K	2646	2681	2656	2654
Density, kg/m^3	0.375	0.465	0.468	0.489
Mass fraction of Al	0.186	0.174	0.364	0.380
Coolant mass flux, $kg/(m^2 \cdot s)$	0.986	2.23	2.20	2.32
Incident heat flux, MW/m^2	15.05	32.36	13.81	13.81
Evaporative heat flux, MW/m^2	13.66	30.90	12.40	12.40
Radiative heat flux, MW/m^2	1.389	1.465	1.410	1.406
HTC, $kW/(m^2 \cdot K)$	1.87	4.04	1.72	1.72
MTC, m/s	14.1	27.6	12.9	12.5
$T_w/T_{0,\text{inf}}$	0.247	0.251	0.248	0.248
u_0, m/s	−2.63	−4.80	−4.70	−4.74

surface temperature can lead to a large evaporative heat flux. This phenomenon keeps the surface temperature of an evaporative transpiration TPS near the saturation temperature of its coolant and has been observed in previous studies such as [6,17].

However, the exothermic coolant oxidation reaction does increase the coolant mass flux substantially to 2.23 $kg/(m^2 \cdot s)$, a 126% increase over the nonreacting 6-species solution. This is because the exothermic oxidation reaction creates the region of elevated temperature as observed in Fig. 6. The region of elevated temperature increases the temperature gradient inside the boundary layer significantly, thereby increasing the incident heat flux and required evaporative heat flux by Eq. (21). A larger evaporative heat flux can only be supplied by increasing the coolant mass flux. As a result, the 7-species solutions show a roughly twofold increase in the coolant mass flux and the evaporative heat flux at the stagnation point. Because the surface temperatures between the 6- and 7-species solutions are similar, the radiative heat fluxes also remain similar.

Table 3 also shows an increase in density for the 7-species solution. This is due to the increased mass of coolant injected into the flow with the increased coolant mass flux. However, the stagnation pressure and surface temperature remain similar between the different solutions, as shown in Figs. 3 and 6. The increase in density is offset by the corresponding increase in the flow mixture's molar mass. This balances the right-hand side of the equation of state, such that the stagnation pressure remains nearly unchanged.

The solution for the coolant with the decreased latent heat of vaporization shows the expected twofold increase in the stagnation point mass flux, visible in Table 3. Worth noting is the decrease in both the incident heat flux and evaporative heat flux for this solution when compared to the original 6-species solution. Ko et al. [6] have shown that coolants with smaller latent heats of vaporization create smaller thermal gradients inside the boundary layer. As such, both the incident and evaporated heat flux decrease with decreasing latent heat of vaporization. The required coolant mass flux remains high due to the decreased cooling potential of the coolant with the decreased latent heat of vaporization. Table 3 also shows that the mass fraction of aluminum for the solution with the decreased latent heat of vaporization is larger than solutions considering aluminum's accepted latent heat. This is due to the larger coolant mass flux required of the less potent coolant material.

The solution with the increased molar mass of coolant shows very similar trends as the solution with the decreased latent heat of vaporization. This is consistent with the results from Ko et al. [6]. The most significant difference between these solutions is in the slightly larger surface density, mass fraction of aluminum, and required coolant mass flux in the solution with the increased molar mass. This is because the coolant with the increased molar mass differs from the properties of aluminum by a factor of 2.6 rather than a factor of 2.5. This leads to more exaggerated changes in the solution with the increased molar mass as this property was changed more. These relationships are highly nonlinear and interdependent, and different properties were adjusted between the two solutions. As a result, the solutions with the increased molar mass and decreased latent heat do not differ proportionally to how their coolant material properties were altered.

The HTC and MTC are reported in Table 3. For both the HTC and MTC, the case with increased molar mass has the lowest value, followed by the case for decreased latent heat of vaporization, then the 6-species solution, and finally the 7-species solution has the highest HTC and MTC. This ordering of the HTC and MTC can be explained by the relationship between the evaporative heat flux and the HTC and MTC. The evaporative heat flux is the main heat flux balancing the incident heat flux in Eq. (21) and sets the demand for the coolant mass flux by influencing the surface temperature in Eqs. (23) and (24). Therefore, the change in the HTC and MTC between the 6- and 7-species solutions is roughly proportional to the change in the required coolant mass flux. The steeper temperature gradient in the 7-species solution, as observed with Fig. 6, is responsible for a larger incident heat flux, which in turn necessitates the larger HTC.

Additionally, the solutions with increased molar mass and decreased latent heat of vaporization have similar HTC and MTC because they have similar evaporative coolant fluxes, and their properties were varied by nearly the same factor. The molar mass varied slightly more than the latent heat of vaporization, so the solution with increased molar mass has the lowest HTC and MTC by a slight margin. The flow velocity at the stagnation point can be seen to increase with increased coolant mass flux and MTC.

The stagnation point velocity is within an order of magnitude of the MTC for each solution, showing that the values of the MTC reported are physical and not unreasonably large or small. It is reasonable that the MTC is larger than the flow velocity, as the diffusion velocity of aluminum is larger than the bulk velocity at the stagnation point, as shown in Fig. 8. As a reference, the diffusion velocity of aluminum is −22.6 m/s and the species velocity of aluminum is −27.4 m/s at the stagnation point for the 7-species solution. The negative velocities signify flow upstream, away from the leading-edge surface, as with Fig. 8.

The ratio of the incident heat flux to the required mass flux should be roughly proportional to the latent heat of vaporization of the coolant on a per-mass basis (kJ/kg) in order for the vaporization of coolant to absorb the incident heat flux as per Eq. (21). The ratio of the HTC to MTC remains similar for all cases, showing this proportional relationship. The maximum HTC for the vaporization of water is around 2×10^4 $(W/m^2 \cdot K)$ as reported by Narayan et al. [48] and Stephan et al. [49]. Due to aluminum having a larger latent heat of vaporization than water, it is expected that the maximum HTC for the 6-species case should be on the order of magnitude of approximately 0.1 (MW/m^2). The results for the HTC are therefore confirmed to be less than this approximate maximum value. The reported values of the HTC are far smaller than this approximate maximum, as discussed with Eq. (14). This is due to the physical differences between traditional boiling phase change and the vaporization of coolant along a hypersonic leading edge and the different temperatures used to calculate the HTC as a result. The freestream stagnation temperature for this flow, Mach 15 and 30 km altitude, is

10,669 K. The ratio of the wall temperature to the freestream stagnation temperature is also reported in Table 3, with values similar to those of Lin and Nagamatsu [42] and Nagamatsu et al. [43], among other studies.

Figure 9 shows the mass flux of aluminum along the leading-edge surface for the 7-species reacting solution, the 6-species nonreacting solution, and both of the 6-species nonreacting solutions with decreased heat of formation and increased molar mass. The leftmost boundary is the stagnation location, and traveling rightward corresponds to traveling circumferentially along the leading-edge surface.

Figure 9 illustrates the trend in coolant mass flux at the stagnation point observed in Table 3. The coolant mass flux decreases downstream of the stagnation point. This is expected as the surface heating becomes less severe further away from the stagnation point. The supplied coolant mass flux is balanced by diffusion of coolant away from the surface as discussed with Fig. 8. The partial pressure of aluminum is thereby maintained slightly below the saturation pressure of aluminum downstream the leading-edge surface as discussed with Fig. 3 and Eq. (23). The 6-species nonreacting solutions with decreased heat of formation or increased molar mass experience an increase in the required coolant mass flux when compared with the solutions of the nonreacting aluminum coolant. The decreased cooling potential per unit mass of these coolants leads to larger required coolant mass fluxes and larger quantities of coolant vapor. The original 6-species nonreacting solution maintains a coolant mass flux of roughly half of the other solutions along the entire surface owing to its smaller required coolant mass flux.

The results in this section show a roughly twofold increase in the required coolant mass flux at the stagnation point due to the exothermic oxidation reaction. This increase is roughly equivalent to a reduction in the coolant latent heat of vaporization by a factor of 2.5 or an increase in the coolant molar mass by a factor of 2.6. The performance drawbacks of using a coolant susceptible to oxidation are significant, and the effects of oxidation must be accounted for during design. Due to its low molar mass and high latent heat of vaporization, however, aluminum and similar materials remain competitive when compared with other coolants studied in Ref. [6].

V. Impact of Reaction Speed

In order to further explore how oxidation reactions impact the performance of evaporative transpiration TPS, a study is conducted varying the reaction rate coefficient $C_{f,c}$ as found in Eq. (7) of the aluminum oxidation reaction (R4). Reaction rate data for various oxidation reactions are presented by Johnston and Cohen [38,39]. The value of the reaction rate coefficient for the oxidation of aluminum reaction is reported to be $C_{f,c} = 2 \times 10^{10}$. Typical reaction rate coefficients for oxidation of atomic species range as low as $C_{f,c} \sim 10^{6}$, while reaction rate coefficients for oxidation of molecular species range as low as $C_{f,c} \sim 10^{1}$. Additionally, the exponent η_c in Eq. (7) typically ranges from $\eta_c = -0.9$ to $\eta_c = 2.8$. An η_c of zero is reported for the oxidation of aluminum reaction. With $\eta_c = -0.9$, the reaction speed is lowered nearly proportionally with the surface temperature when compared to a case where η_c is zero. Therefore, with surface temperatures on the order of magnitude of 1000 K, the low end of the reaction rate coefficients considered in this study is reduced three orders of magnitude lower than the value of $C_{f,c} \sim 10^{1}$, while η_c is left as zero. This value of $C_{f,c} \sim 10^{-2}$ thereby represents the slowest feasible oxidation reaction, roughly equivalent to $C_{f,c} \sim 10^{1}$ and $\eta_c = -0.9$ with a surface temperature on the order of magnitude of 1000 K. The value of $C_{f,c} \sim 10^{-2}$ is conservatively low, requiring both the lowest possible values of $C_{f,c}$ and η_c for an oxidation reaction of a molecular species to be feasible.

Still, the reaction rate coefficient was varied by two orders of magnitude around the value of $C_{f,c} \sim 10^{-2}$ to further explore the behavior of the reaction near this region. Therefore, the values of the reaction rate coefficient are varied from their full value of $C_{f,c} = 2 \times 10^{10}$ to a value of 2×10^{-4}. A value of $C_{f,c} = 2 \times 10^{13}$ is also included to determine how a faster reaction would affect the performance of an evaporative transpiration TPS. The zero reaction rate of the nonreacting 7-species study from the validation section is included as well. Results for higher reaction rate coefficients are focused on through most of this section because they are more physically relevant, but the results for lower reaction rates are still included in figures when discussion is warranted.

Figures 10–12 present separate subplots of the mass fractions of different reacting species along the stagnation line for the different reaction rates considered. The x-axis in these figures is rescaled to be normalized as a percentage of the standoff distance of the shock, allowing for direct comparison between different values of the reaction rate coefficient. A semilog axis is used to better illustrate trends close to the stagnation point. The left and right bounds are the postshock and near-surface locations, respectively. Once again, the colloquial definition of the stagnation point, being located at the surface, is used here despite a nonzero surface velocity.

Figures 10–12 illustrate that for reaction rate coefficients of $C_{f,c} \geq 2 \times 10^{4}$, there is no substantial change in the production of aluminum oxide. Additionally, for all solutions with $C_{f,c} \geq 2 \times 10^{4}$, all oxygen in the flow reacts to form aluminum oxide by a

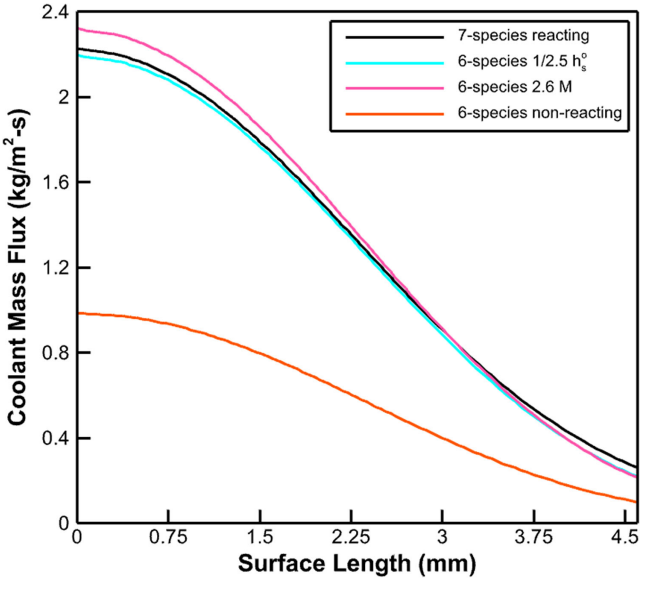

Fig. 9 Surface plot the of coolant mass flux.

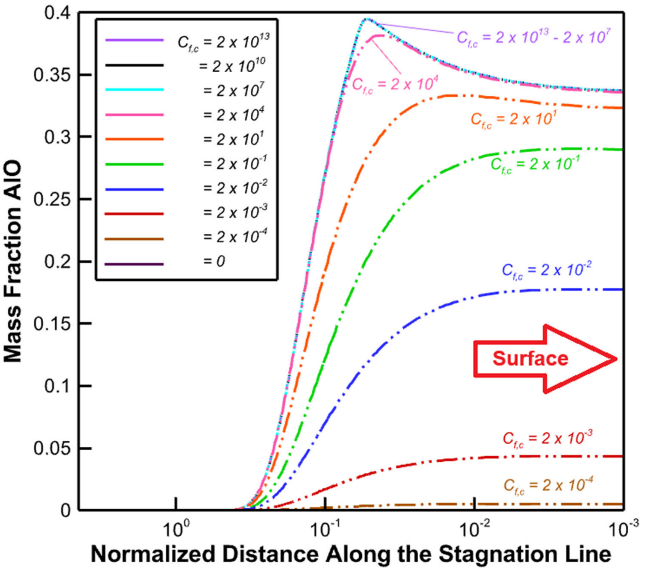

Fig. 10 Normalized stagnation line profiles of the species mass fraction of AlO for varying reaction rates.

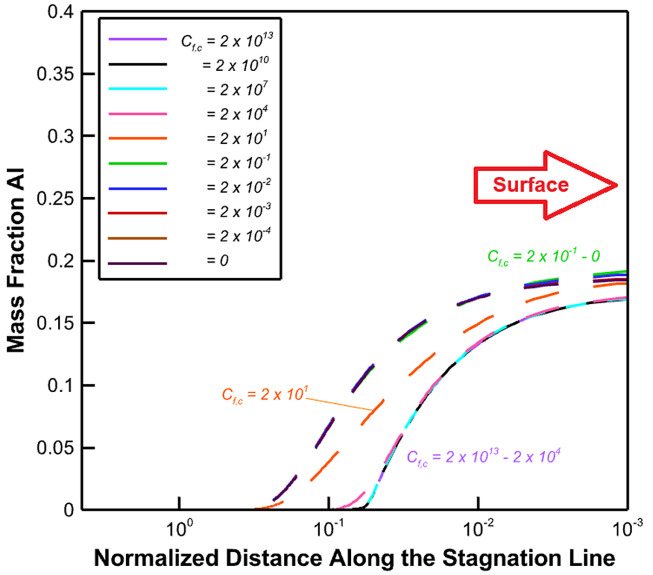

Fig. 11 Normalized stagnation line profiles of the species mass fraction of Al for varying reaction rates.

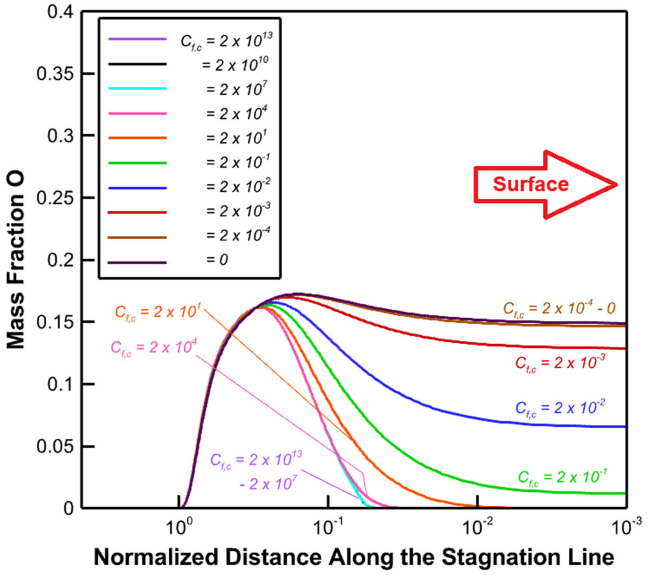

Fig. 12 Normalized stagnation line profiles of the species mass fraction of O for varying reaction rates.

normalized distance of about 0.06, or approximately 20 micrometers away from the stagnation point. This observation suggests that the flow variables are not sensitive to increasing the reaction rate coefficient above $C_{f,c} = 2 \times 10^{4}$.

For a reaction rate coefficient of $C_{f,c} = 2 \times 10^{1}$, the species concentrations along the stagnation line begin to change. A slight decrease in the maximum value of aluminum oxide's mass fraction is observed, and the location of the maximum aluminum oxide concentration moves closer toward the stagnation point. The concentration of oxygen remains above zero closer to the stagnation point as well, but all oxygen is still consumed upstream of the stagnation point. This suggests a completed reaction by the time the flow reaches the leading-edge surface. The mass fraction of aluminum remains greater than zero further away from the stagnation point than for cases with faster reaction rate coefficients.

For a reaction rate coefficient of $C_{f,c} \leq 2 \times 10^{-1}$, the surface concentration of aluminum oxide is at or near its maximum value at the stagnation point. This leads to a flat concentration gradient of aluminum oxide near the stagnation point for these cases. This suggests that the maximum production of aluminum oxide is occurring along the leading-edge surface for the lower reaction rate coefficients. Additionally, the mass fraction of the aluminum profile at these reaction rate coefficients matches the profile for all lower reaction rate coefficients. The mass fraction of oxygen is less than five percent at the stagnation point but still visibly above zero. For a reaction rate coefficient of $C_{f,c} = 2 \times 10^{-2}$, oxygen and aluminum coexist with aluminum oxide at the stagnation point. The stagnation point mass fraction of oxygen is 0.067, as seen in Fig. 12.

Moving to a reaction rate coefficient of $C_{f,c} = 2 \times 10^{-3}$, the oxidation reaction nearly halts. Only a small amount of aluminum oxide is formed, with a mass fraction of 0.044 at the stagnation point. Nearly all of the atomic oxygen reaches the stagnation point. Therefore, a reaction rate coefficient of $C_{f,c} = 2 \times 10^{-3}$ can be considered the highest reaction rate value for the oxidation reaction to remain chemically frozen, with results nearly identical to the nonreacting solutions.

The reactions exhibit a dramatic change over a small range of reaction rate coefficients, consuming all oxygen for $C_{f,c} \geq 2 \times 10^{1}$, but acting chemically inert in a frozen state for $C_{f,c} \leq 2 \times 10^{-3}$. As a note, $C_{f,c} = 2 \times 10^{-3}$ is below the minimum feasible reaction rate coefficient of $C_{f,c} = 2 \times 10^{-2}$. Finally, for a reaction rate coefficient of $C_{f,c} = 2 \times 10^{-4}$, the mass fractions of reacting species are indistinguishable from the nonreacting case.

Then, for a favorable equilibrium constant with reactant species present, as shown in Ko et al. [6], oxidation reactions will occur for any feasible reaction rate. If these conditions are not met, then the reaction does not occur and can be neglected entirely. For a reaction rate coefficient as small as $C_{f,c} = 2 \times 10^{-1}$, 10^{-11} times lower than its accepted value, oxidation of aluminum coolant is significant, and there is near-complete consumption of oxygen species. The slowest feasible reaction rate coefficient is only an order of magnitude lower than this and still leads to substantial production of aluminum oxide and consumption of oxygen by the time the flow reaches the leading-edge surface. Therefore, even extremely slow oxidation reactions cannot be neglected if their equilibrium constant is large. Only unfeasibly slow oxidation reactions lead to frozen flow conditions.

Figure 13 presents the temperature and vibrational temperature along the stagnation line for selected reaction rate coefficients. Only select values of $C_{f,c}$ are plotted for clarity. The values of $C_{f,c}$ plotted correspond to the values from Figs. 10–12 that best cover the distribution of the different reaction rate conditions for equilibrium, nonequilibrium, and frozen flow. The x-axis in Fig. 13 is normalized as a percentage of the standoff distance of the shock,

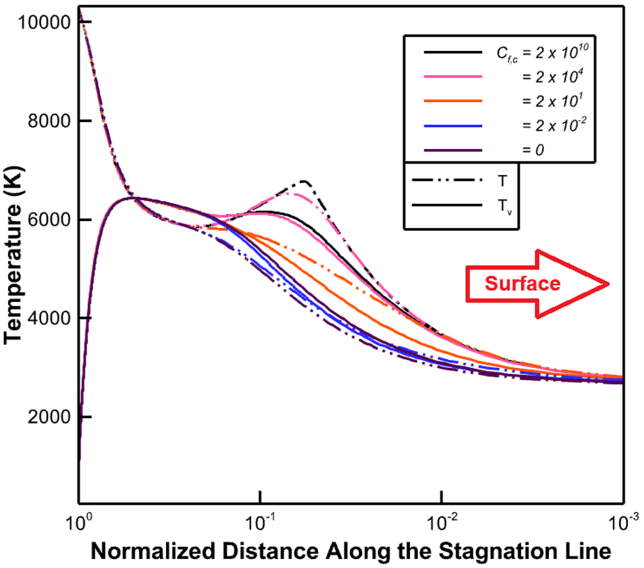

Fig. 13 Normalized stagnation line profiles of the temperature and vibrational temperature for different reaction rates.

allowing for direct comparison between different values of the reaction rate coefficient. The normalized distance is plotted on a semilog scale to clearly illustrate results near the stagnation point. The left and right bounds are the postshock and near-surface locations, respectively.

Figure 13 depicts a region of elevated temperature for reaction rate coefficients of $C_{f,c} \geq 2 \times 10^4$, roughly 2500 K above the nonreacting solution. This maximum temperature occurs at the same location as the maximum concentration of aluminum oxide, as discussed with Fig. 6. A temperature increase at this location is expected due to the exothermic nature of aluminum oxide production and is responsible for dramatically increasing the incident heat flux as previously discussed.

For a reaction rate coefficient of $C_{f,c} = 2 \times 10^1$, the region of elevated temperature is approximately 1000 K above the nonreacting solution, though the temperature gradient near the stagnation point is similar to that of higher reaction rate coefficients. As discussed with Figs. 10, 11, and 12, the location of maximum aluminum oxide concentration occurs closer to the stagnation point and drops off further upstream. This confines the effects of aluminum oxide formation near the surface. Because the concentration of aluminum oxide near the surface is about the same for $C_{f,c} = 2 \times 10^1$ and for higher reaction rate coefficients, the heat released due to the reaction and the heat that is carried to the surface remain similar. Therefore, the incident heat flux is similar between these solutions despite the smaller overall temperature increase and the lower temperature gradient further upstream of the leading-edge surface. The lower reaction rates exhibit temperature profiles along the stagnation line similar to the nonreacting case.

The vibrational temperature also changes similarly, as the region of elevated temperature in turn leads to greater molecular excitation. The effect on vibrational temperature is not as pronounced, however, as the nonequilibrium state of vibrational excitation causes the vibrational temperature to lag behind the changes in the translational-rotational temperature.

Table 4 details how the performance of evaporative transpiration TPS are affected by changes in the reaction rate coefficient. Additionally shown is the equilibrium constant and chemical equilibrium ratio at the stagnation point for each reaction rate coefficient. Once again, the colloquial definition of the stagnation point, being located at the surface, is used here despite a nonzero surface velocity. The equilibrium constant and chemical equilibrium ratio were taken one grid point away from the leading-edge surface so that the aluminum vapor would have a finite length of time to react in the flow.

Table 4 shows that, for the minimum feasible reaction rate coefficient of $C_{f,c} \geq 2 \times 10^{-2}$, the oxidation reaction is significant, and additional coolant is required to replace the coolant that is oxidized. By $C_{f,c} = 2 \times 10^1$, the maximum coolant mass flux at the stagnation point is required of the transpiration TPS. This is because, as discussed with Figs. 10, 11, and 12, there is near-complete consumption of oxygen for this reaction rate coefficient. Complete consumption of oxygen corresponds to the maximum possible energy release by the reaction because the reaction cannot progress past this state without consuming more oxygen. Release of energy from the oxidation reaction leads to an increased incident heat flux. The similar incident heat fluxes for $C_{f,c} = 2 \times 10^1$ and larger reaction rate coefficients discussed with Fig. 13 lead to the similar required coolant mass fluxes.

For a reaction rate coefficient of $C_{f,c} = 2 \times 10^{-1}$, the effects of the oxidation reaction are less pronounced. The aluminum vapor coexists with some oxygen near the stagnation point, visible in Figs. 10, 11, and 12. The reaction rate coefficient of $C_{f,c} = 2 \times 10^{-1}$ shows a required coolant mass flux similar to that of the faster reaction rate cases because most, but not all, of the oxygen is consumed by the time the flow reaches the stagnation point. For $C_{f,c} = 2 \times 10^{-2}$, the required coolant mass flux is between the nonreacting and equilibrium reaction mass fluxes, due to even less consumption of oxygen. As a note, the mass flux for $C_{f,c} = 2 \times 10^{-3}$ is 1.15 $\mathrm{kg/(m^2 \cdot s)}$. This value is slightly larger than the results for nonreacting flow because the oxidation reaction still occurs for a finite reaction rate coefficient, although at a slow and nearly insignificant rate.

Table 4 shows a favorable equilibrium constant for the formation of aluminum oxide, as per reaction (R4), in all applicable cases. Regardless, for reaction rate coefficients of $C_{f,c} \geq 2 \times 10^7$, the chemical equilibrium ratio at the stagnation point is one. This shows that the reactions are in chemical equilibrium at the stagnation point. For a reaction rate coefficient of $C_{f,c} = 2 \times 10^4$, the chemical equilibrium ratio is slightly greater than one. This suggests that there is too much aluminum vapor and not enough aluminum oxide near the leading-edge surface to perfectly represent a state of chemical equilibrium. The chemical equilibrium ratio at the stagnation point increases rapidly for decreasing reaction rate coefficients of $C_{f,c} \leq 2 \times 10^1$, suggesting nonequilibrium flow conditions.

Figures 14 present plots of the chemical equilibrium ratio (a) and the chemical timescale ratio (b) along the stagnation line for varying reaction rate coefficients. The x-axis in each figure is normalized as a percentage of the standoff distance of the shock, allowing for direct comparison between different values of the reaction rate coefficient. The results are plotted on log-log scales to better illustrate the data. The left and right bounds are the postshock and near-surface locations, respectively. Only select values of $C_{f,c}$ are plotted for clarity. The values of $C_{f,c}$ plotted correspond to the values from Figs. 10, 11, and 12 that best cover the distribution of the different reaction rate conditions for equilibrium, nonequilibrium, and frozen flow.

The chemical equilibrium ratio along the stagnation line is one or near one for reaction rate coefficients of $C_{f,c} \geq 2 \times 10^4$. For $C_{f,c} = 2 \times 10^4$, the chemical equilibrium ratio does increase to around 100 at the location of the maximum concentration of aluminum oxide. This shows that at this location there is a momentary lack of formation of aluminum oxide and deviation from equilibrium conditions. However, the chemical equilibrium ratio quickly decreases near the stagnation point, showing that the reaction eventually progresses to near completion and achieves a near-equilibrium state similar to the faster reactions. The diffusion of aluminum oxide away from the point of maximum aluminum oxide concentration, as shown with Fig. 8, assists in maintaining equilibrium conditions near the leading-edge surface by increasing the concentration of aluminum oxide there.

For a reaction rate coefficient of $C_{f,c} = 2 \times 10^1$, the chemical equilibrium ratio at the stagnation point is well above one and increases further upstream to a value near 10,000. The large chemical equilibrium ratio observed in Fig. 14 corresponds with deviation from equilibrium conditions and the coexistence of all reacting species along a significant portion of the stagnation line, as visible in Figs. 10, 11, and 12. For $C_{f,c} = 2 \times 10^1$ there is still nearly complete consumption of oxygen and significant formation of aluminum oxide by the time the flow reaches the surface despite the large chemical equilibrium ratio.

Figure 14 shows that the distribution of chemical timescale ratios along the stagnation line remains similar for reaction rate coefficients of $C_{f,c} > 2 \times 10^4$. The maximum chemical timescale ratio

Table 4 Comparison of the stagnation point properties for different reaction rates

$C_f, c = 2x$	10^{13}	10^{10}	10^7	10^4	10^1	10^{-1}	10^{-2}	0
Coolant mass flux, $\mathrm{kg/m^2 \cdot s}$	2.23	2.23	2.23	2.23	2.23	2.14	1.67	0.987
Equilibrium constant, $\mathrm{nmol/m^3}$	95.4	95.4	95.5	95.5	102	101	85.4	NA
Chemical equilibrium ratio	1.00	1.00	1.00	1.31	797	3.32×10^6	33.5×10^6	NA

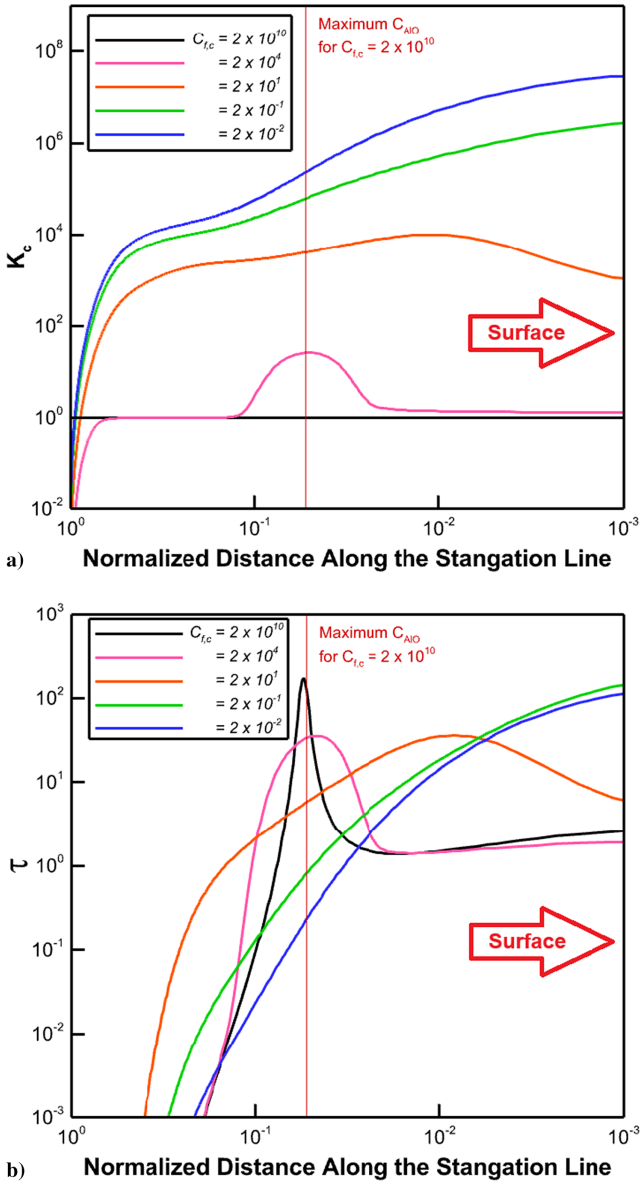

Fig. 14 Chemical equilibrium (a) and timescale ratio (b) for different reaction rates.

corresponds with the location of the maximum value of the chemical equilibrium ratio and the maximum concentration of aluminum oxide, as seen in Fig. 10. This is because the location of the maximum chemical timescale corresponds to the location with maximum production of aluminum oxide as per Eq. (12). The chemical timescale ratio near the stagnation point generally increases with decreasing reaction rate coefficient until a maximum timescale ratio is reached at $C_{f,c} = 2 \times 10^{-4}$.

The faster reactions show lower chemical timescale ratios near the stagnation point because the reaction has already reached completion by the time the flow reaches the stagnation point. This results in a lower value for the concentration of oxygen and a decreased chemical source term, which in turn decreases the chemical equilibrium ratio and chemical timescale ratio, respectively, as per Eqs. (11) and (12). For a reaction rate coefficient of $C_{f,c} = 2 \times 10^4$, the chemical timescale ratio near the stagnation point can be observed to decrease when compared with faster reactions. It is speculated that because the leading-edge surface is still in a state of near equilibrium and because the reaction center remains far away from the stagnation point, the lower reaction rate coefficient of $C_{f,c} = 2 \times 10^4$ leads to a lower chemical source term and chemical timescale ratio when compared to faster reactions. The chemical timescale ratio near the stagnation point then begins to increase with decreasing reaction rate coefficient as the reaction center moves closer toward the stagnation point. This trend persists until $C_{f,c} \leq 2 \times 10^{-1}$.

For a reaction rate coefficient of $C_{f,c} \leq 2 \times 10^{-1}$, the chemical equilibrium ratio and chemical timescale ratio both have maximums at the stagnation point. This is due to the location of the maximum concentration of aluminum oxide moving closer toward the stagnation point as the reaction speed slows down. This is supported by the constant and elevated mass fraction of atomic oxygen near the stagnation point, not reacting in the presence of aluminum, observable in Figs. 10, 11, and 12. For $C_{f,c} \leq 2 \times 10^{-1}$, despite a large chemical equilibrium ratio and a large chemical timescale ratio near the stagnation point, the overall reaction rate along the rest of the stagnation line remains insufficient to produce aluminum oxide. The chemical timescale constant drops too low to produce significant quantities of aluminum oxide around the normalized location of 10^{-2} along the stagnation line, about 1% the length of the stagnation line. If nonequilibrium effects are prevalent at the stagnation point, then they will only be stronger further upstream. This can be seen by the chemical timescale ratio dropping below a value of one upstream of around 2% of the length of the stagnation line, indicating a transition to frozen flow conditions.

Then, the timescale ratio begins to decrease for $C_{f,c} = 2 \times 10^{-2}$ because the reaction center cannot move closer toward the stagnation point to give oxygen and aluminum more time to react, as in Fig. 14. A decrease in the reaction rate coefficient is thereby reflected as a decrease in the chemical timescale ratio for reaction rate coefficients below $C_{f,c} = 2 \times 10^{-1}$.

Therefore, the chemical timescale ratio at the stagnation point generally increases as the nonequilibrium effects become more significant and the reaction center moves closer toward the leading-edge surface, despite decreasing the reaction rate coefficient. If the reaction is already occurring at the surface or is in a state of equilibrium with the reaction center far from the surface, then the chemical timescale ratio increases for increasing reaction rate coefficient.

As discussed with Fig. 8, the diffusion of aluminum oxide must be directed away from the location of maximum aluminum oxide production. Therefore, for $C_{f,c} \leq 2 \times 10^{-1}$, diffusion cannot assist in increasing the surface concentration of aluminum oxide because the reaction center is near the stagnation point. There is insufficient concentration of reacting species near the shock for the chemical equilibrium ratio or chemical timescale ratio to be physically meaningful there.

This analysis shows that the flow remains in a state of equilibrium for reaction rate coefficients as low as $C_{f,c} = 2 \times 10^4$. Even for a reaction rate coefficient as low as $C_{f,c} = 2 \times 10^{-2}$, which exhibits nonequilibrium flow conditions, the required coolant mass flux of the evaporative transpiration TPS changes by 70% of the difference between the cases with faster reaction rate coefficients and the nonreacting coolant. The range of reaction rates where nonequilibrium effects are significant is so small that it is reasonable to assume that oxidation reactions occur in either equilibrium or frozen conditions.

If the maximum chemical equilibrium and timescale ratio occur at the leading-edge surface, then the nonequilibrium effects will begin to influence the required coolant mass flux. This result is observable in Table 4 and Fig. 14. If the maximum chemical equilibrium and timescale ratio occur away from the leading-edge surface, then the oxidation reaction will increase the required coolant mass flux by the maximum possible amount. The diffusion of aluminum oxide toward the leading-edge surface can assist in maintaining equilibrium conditions near the leading-edge surface by increasing the concentration of aluminum oxide there, but only so long as the reaction center is located away from the surface.

Therefore, transpiration TPS are mainly affected by the energy released by the reaction between oxygen and metallic coolant. Even for nonequilibrium flow conditions that may be present for the slowest feasible reactions, the majority of oxygen can be consumed

by an oxidation reaction by the time the flow reaches the leading-edge surface. This leads to the same or similar impact on TPS performance as the equilibrium conditions observed with the faster reaction rate coefficients. This idea is further supported by the dependence of the required coolant mass flux on the temperature gradient only at the stagnation point as observed with Fig. 6. Therefore, for the reaction to be significant to the performance of evaporative transpiration TPS performance, the reaction does not need to be instantaneous or in an equilibrium state along the stagnation line. If a nonequilibrium reaction has consumed a majority of the oxygen in the flow at the stagnation point, then the reaction's impact on TPS performance will be largely the same as for an equilibrium reaction. Oxidation reactions must be taken into account, as even the slowest feasible oxidation reactions have a substantial effect on the performance of evaporative transpiration TPS.

Figure 15 presents the resulting incident and evaporative heat fluxes along the leading-edge surface as the reaction rate coefficient is varied. Additionally shown is the cooling heat flux for comparison to the incident heat flux. The cooling heat flux is defined as the evaporative heat flux plus the radiative heat flux. Other heat fluxes, such as the radiative heat flux or recombination heat flux, are not explicitly shown because they are either nearly constant between trials or insignificant. The leftmost boundary is the stagnation location, and traveling rightward corresponds to traveling circumferentially along the leading-edge surface.

Previous results are reinforced through Fig. 15. The region of elevated temperature from Fig. 13 leads to an increase in the temperature gradient inside the boundary layer and therefore an increase in the incident heat flux by Eq. (21). The evaporative heat flux must then increase to counteract the increased incident heat flux caused by the exothermic oxidation reaction. This balancing of heat fluxes keeps the surface temperature near the saturation temperature of the coolant, as required by Eqs. (23) and (24), but increases the required coolant mass fluxes as reported in Table 4. These processes can be seen to relate visually in Fig. 15. A change in the reaction rate coefficient leads to a change in both the incident and evaporative heat fluxes. A change in the incident heat flux is offset by an equal change in the evaporative heat flux and vice versa, as the other heat fluxes do not change significantly. The incident and cooling heat fluxes can be seen to be equal in all cases.

Once again, all results with a large reaction rate coefficient are similar. The surface heat fluxes do not begin to substantially distinguish themselves until $C_{f,c} \leq 2 \times 10^{-2}$. This corresponds to the coolant mass flux values reported in Table 4. The coolant mass fluxes for reaction rates of $C_{f,c} \geq 2 \times 10^{-1}$ are all roughly equivalent and only begin to distinguish themselves for $C_{f,c} \leq 2 \times 10^{-2}$

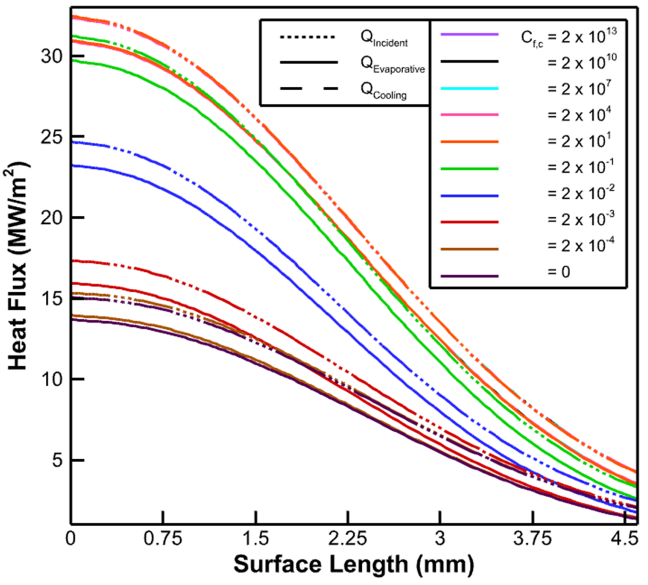

Fig. 15 Surface heat fluxes for different reaction rates.

due to the nonequilibrium effects present at the stagnation point as discussed with Fig. 14. The nonequilibrium effects are not significant at the stagnation point for the faster reactions, as discussed with Fig. 14.

For reaction rate coefficients of $C_{f,c} \leq 2 \times 10^{-3}$, the reaction becomes frozen, and so the incident and cooling heat fluxes match the nonreacting case closely. Additionally, the profile of the heat fluxes shown in Fig. 15 matches with the profiles of pressure and mass flux shown in Figs. 3 and 9. This is because the surface pressures influence the coolant mass flux rate by Eq. (23), which directly influences the cooling heat flux, which is determined by the incident heat flux as governed by Eq. (21).

Based on these results, if the conditions for an oxidation reaction to occur are met, then the oxidation reaction will lead to an increase in the incident heat flux along the leading-edge surface. Oxidation reactions are expected to occur in, or as if in, an equilibrium state. This leads to the complete consumption of oxygen and the maximum amount of heat released at the stagnation point. This results in an increase in both the evaporative heat flux and the coolant mass flux, while the surface temperature remains nearly unchanged. Even for the slowest feasible reaction rates, the nonequilibrium effects are not strong enough to alleviate the increase in the required coolant mass flux caused by an oxidation reaction.

Because the flowfield in this study is oxygen-depleted near the leading-edge surface, oxidation reactions not considered in this study may be of importance. A specific reaction of interest is the formation of aluminum(I) oxide, Al_2O, expected to form in significant quanities due to the oxygen-depleted flow environment. Formation of this oxide may have a significant impact on evaporative transpiration TPS performance, as twice the additional aluminum may be required to form this oxide as is required to form aluminum oxide, AlO, considered in this study. Finally, oxidation reactions occurring at low altitudes may be more susceptible to nonequilibrium effects, as there is more oxygen to be consumed in a denser flow.

VI. Conclusions

Because one of the main limiting design considerations for hypersonic flight vehicles is the severe incident heat fluxes present during atmospheric hypersonic flight, research into more effective TPS is desired. Evaporative transpiration TPS are desirable because they function without degrading the leading-edge surface and can maintain sharp leading-edge geometry for high lift-to-drag ratios.

Evaporative transpiration TPS have been shown to be effective at combating incident heat fluxes up to 85 MW/m^2 by Ko et al. (2024) [6]. However, the effectiveness of coolant materials that may undergo oxidation was in question. This study expands on the work of Ko et al. [6] to further explore the limits of evaporative transpiration TPS. Specifically, this study investigates the effects of exothermic coolant oxidation reactions on evaporative transpiration TPS performance. This is accomplished through DNS studies of an evaporative transpiration TPS employing aluminum as the coolant material along the leading edge of a 3.1 mm nose tip radius flying at Mach 15 and an altitude of 30 km. The exact quantitative accuracy of these results may be effected by the assumption that the vibrational characteristics of aluminum oxide are approximated as those of silicon oxide; however, the trends observed as a result of the oxidation reactions in this study are still valid.

After the initial validation study of the new DNS code used to simulate the evaporative transpiration TPS, the effect of coolant oxidation on the performance of the evaporative transpiration TPS was investigated. It is found that coolant oxidation leads to roughly a twofold increase in the required coolant mass flux at the stagnation point, while the surface temperature remains nearly unchanged. The increased coolant mass flux is caused by an increased incident heat flux due to the exothermic oxidation reaction. Therefore, if the coolant may oxidize, the effects of coolant oxidation must be accounted for during the design of evaporative transpiration TPS. The twofold increase in the required coolant mass flux caused by coolant oxidation is roughly

equivalent to a reduction in the coolant's latent heat of vaporization by a factor of 2.5 or an increase in the coolant's molar mass by a factor of 2.6.

The relationship between the reaction rate of coolant oxidation reactions and the performance of evaporative transpiration TPS is also investigated. It is shown that oxidation reactions are likely to remain in a state of equilibrium or near equilibrium, even for the slowest feasible reactions. This is because the nonequilibrium effects are significant over a narrow range of slow reaction rates, spanning three orders of magnitude for the reaction rate coefficient out of the span of 18 orders of magnitude considered.

Even for reaction rates as low as 10^{-11} times their accepted values, conditions still heavily favor coolant oxidation, resulting in complete or nearly complete consumption of oxygen. Even in flows exhibiting nonequilibrium conditions, nearly all oxygen in the flow reacts and releases energy by the time the flow reaches the stagnation point. This leads to a similar change in the incident heat flux and required coolant mass flux for both equilibrium and nonequilibrium flows.

Even the slowest feasible oxidation reactions dramatically affect evaporative transpiration TPS performance, increasing the surface heat flux and required coolant mass flux by roughly a factor of two compared with a nonreacting coolant. Because oxidation reactions occur so readily and have a substantial impact on evaporative TPS performance, the oxidation of coolant species must be considered during the design of evaporative transpiration TPS. While the performance drawbacks of coolant oxidation are significant, oxidizing coolants may still be viable if their latent heats of vaporization are double that of alternative coolants, or if their molar masses are half that of alternative coolants. With these results, a step has been taken toward one day implementing evaporative transpiration TPS capable of providing large cooling fluxes without degradation of the leading-edge surface.

Acknowledgments

Computations were run on Purdue ANVIL, with computational time granted via the Advanced Cyberinfrastructure Coordination Ecosystem: Services & Support (ACCESS) program. Without the core-hours and computational resources provided, this research could not have been completed. We also acknowledge the SMART Scholarship program, the Under Secretary of Defense-Research and Engineering (OUSD/R&E), the National Defense Education Program (NDEP)/BA-1, Basic Research, W911NF-22-2-0156, for providing funding during the completion of the research. The content and conclusions of this paper are those of the authors and do not necessarily represent the views of the supporting organizations acknowledged here. A. Mannion also thanks ChatGPT, Copilot, Grammarly, and Writeful as artificial intelligence tools used to assist in correcting grammatical and spelling mistakes in rough drafts of this work.

References

[1] Van Driest, E. R., *The Problem of Aerodynamic Heating*, Inst. of the Aeronautical Sciences, Los Angeles, CA, 1956, pp. 26–41.

[2] Fay, J. A., and Riddell, F. R., "Theory of Stagnation Point Heat Transfer in Dissociated Air," *Journal of the Aerospace Sciences*, Vol. 25, No. 2, 1958, pp. 73–85. https://doi.org/10.2514/8.7517

[3] Tran, H., Johnson, C., Rasky, D., Hui, F., Hsu, M.-T., and Chen, Y., "Phenolic Impregnated Carbon Ablators (PICA) for Discovery Class Missions," *31st Thermophysics Conference*, AIAA Paper 1996-1911, 1996. https://doi.org/10.2514/6.1996-1911

[4] Meurisse, J. B. E., Chatzigeorgis, G. B., Diaz, P. V., Bessire, B. K., Panerai, F., and Mansour, N. N., "Equilibrium Model for the Ablation Response of Silicone-Coated PICA," *International Journal of Heat and Mass Transfer*, Vol. 201, 2023, Paper 123523. https://doi.org/10.1016/j.ijheatmasstransfer.2022.123523

[5] Anderson, J. D., Jr., *Modern Compressible Flow: With Historical Perspective*, McGraw-Hill, New York, 2004.

[6] Ko, D., and Mannion, A., "Parametric Study of Transpiration Cooling Using Oxides for Sharp Hypersonic Leading Edges," *Journal of Thermophysics and Heat Transfer*, Vol. 39, No. 1, 2024, pp. 38–52. https://doi.org/10.2514/1.T6991

[7] Sahu, R., Tropina, A., Andrienko, D., and Miles, R., "Cesium Seeding for Effective Electron Transpiration Cooling in Hypersonic Flows," *Plasma Sources Science and Technology*, Vol. 31, No. 3, 2022 Paper 035001. https://doi.org/10.1088/1361-6595/ac4ecc

[8] Weston, K. C., "The Stagnation-Point Boundary Layer with Suction and Injection in Equilibrium Dissociating Air," NASA TN D-3889, Manned Spacecraft Center, Houston, TX, Dec. 1968.

[9] Henline, W. D., "Transpiration Cooling of Hypersonic Blunt Bodies with Finite Rate Surface Reactions," TR A-89018, Ames Research Center, Moffett Field, CA, Feb. 1989.

[10] Otsu, H., Fujita, K., and Ito, T., "Application of the Transpiration Cooling Method for Reentry Vehicles," *45th AIAA Aerospace Sciences Meeting and Exhibit*, AIAA Paper 2007-1209, 2007. https://doi.org/10.2514/6.2007-1209

[11] Huang, G., Zhu, Y., Liao, Z., and Jiang, P.-X., "Experimental Investigation of Self-Pumping Internal Transpiration Cooling," *International Journal of Heat and Mass Transfer*, Vol. 123, 2018, pp. 514–522. https://doi.org/10.1016/j.ijheatmasstransfer.2018.02.046

[12] Wu, N., Wang, J., He, F., Chen, L., and Ai, B., "Optimization Transpiration Cooling of Nose Cone with Non-Uniform Permeability," *International Journal of Heat and Mass Transfer*, Vol. 127, 2018, pp. 882–891. https://doi.org/10.1016/j.ijheatmasstransfer.2018.07.134

[13] Gulli, S., and Maddalena, L., "Arc-Jet Testing of a Variable-Transpiration-Cooled and Uncoated Carbon–Carbon Nose Cone," *Journal of Spacecraft and Rockets*, Vol. 56, No. 3, 2019, pp. 780–788. https://doi.org/10.2514/1.A34176

[14] He, F., Wu, N., Ran, F., and Wang, J., "Numerical Investigation on the Transpiration Cooling of Three-Dimensional Hypersonic Inlet," *Aerospace Science and Technology*, Vol. 106, 2020, Paper 106152. https://doi.org/10.1016/j.ast.2020.106152

[15] Ifti, H. S., Hermann, T., McGilvray, M., and Merrifield, J., "Numerical Simulation of Transpiration Cooling in a Laminar Hypersonic Boundary Layer," *Journal of Spacecraft and Rockets*, Vol. 59, No. 5, 2022, pp. 1726–1735. https://doi.org/10.2514/1.A35325

[16] Ewenz Rocher, M., Hermann, T., McGilvray, M., and Gollan, R., "Correlation for Species Concentration on a Hypersonic Stagnation Point with Mass Injection," *AIAA Journal*, Vol. 60, No. 5, 2022, pp. 2798–2809. https://doi.org/10.2514/1.J061159

[17] van Foreest, A., Sippel, M., Gülhan, A., Esser, B., Ambrosius, B. A. C., and Sudmeijer, K., "Transpiration Cooling Using Liquid Water," *Journal of Thermophysics and Heat Transfer*, Vol. 23, No. 4, 2009, pp. 693–702. https://doi.org/10.2514/1.39070

[18] Luo, S., Miao, Z., Liu, J., Song, J., Xi, W., and Liu, C., "Effects of Coolants of Double Layer Transpiration Cooling System in the Leading Edge of a Hypersonic Vehicle," *Frontiers in Energy Research*, Vol. 9, 2021 Paper 756820. https://doi.org/10.3389/fenrg.2021.756820

[19] Scala, S. M., and Vidale, G. L., "Vaporization Processes in the Hypersonic Laminar Boundary Layer," *International Journal of Heat and Mass Transfer*, Vol. 1, No. 1, 1960, pp. 4–22. https://doi.org/10.1016/0017-9310(60)90003-X

[20] Charwat, A. F., "The Effect of Surface-Evaporation Kinetics on Sublimation Near the Leading Edge," *International Journal of Heat and Mass Transfer*, Vol. 8, No. 3, 1965, pp. 383–394. https://doi.org/10.1016/0017-9310(65)90001-3

[21] Kubota, T., "Ablation with Ice Model at $M = 5.8$," *ARS Journal*, Vol. 30, No. 12, 1960, pp. 1164–1169. https://doi.org/10.2514/8.5355

[22] Baker, R. L., "Graphite Sublimation Chemistry Nonequilibrium Effects," *AIAA Journal*, Vol. 15, No. 10, 1977, pp. 1391–1397. https://doi.org/10.2514/3.60806

[23] Faghri, A., *Heat Pipe Science and Technology*, Global Digital Press, Washington, 1995, pp. 221–267.

[24] He, F., and Wang, J., "Numerical Investigation on Critical Heat Flux and Coolant Volume Required for Transpiration Cooling with Phase Change," *Energy Conversion and Management*, Vol. 80, 2014, pp. 591–597. https://doi.org/10.1016/j.enconman.2014.02.003

[25] Mortensen, C. H., and Zhong, X., "Simulation of Second-Mode Instability in a Real-Gas Hypersonic Flow with Graphite Ablation,"

AIAA Journal, Vol. 52, No. 8, 2014, pp. 1632–1652. https://doi.org/10.2514/1.J052659

[26] Mortensen, C. H., and Zhong, X., "Real-Gas and Surface-Ablation Effects on Hypersonic Boundary-Layer Instability over a Blunt Cone," *AIAA Journal*, Vol. 54, No. 3, 2016, pp. 980–998. https://doi.org/10.2514/1.J054404

[27] Dias, B., Turchi, A., Stern, E. C., and Magin, T. E., "A Model for Meteoroid Ablation Including Melting and Vaporization," *Icarus*, Vol. 345, 2020, Paper 113710. https://doi.org/10.1016/j.icarus.2020.113710

[28] Raghunandan, P., Haskins, J. B., Palmer, G. E., Bessire, B. K., and Stern, E. C., "Material Response Modeling of Melt Flow-Vapor Ablation for Iron," *AIAA Journal*, Vol. 60, No. 4, 2022, pp. 2028–2038. https://doi.org/10.2514/1.J060788

[29] Blottner, F. G., Johnson, M., and Ellis, M., "Chemically Reacting Viscous Flow Program for Multi-Component GAS MIXTURES," TR SC-RR-70-754, Sandia Labs, Albuquerque, Jan. 1971, pp. 44–45. https://doi.org/10.2172/4658539

[30] Gupta, R., Lee, K.-P., Moos, J., and Sutton, K., "Viscous-Shock-Layer Solutions with Coupled Radiation and Ablation Injection for Earth Entry," *5th Joint Thermophysics and Heat Transfer Conference*, AIAA Paper 1990-1697, 1990. https://doi.org/10.2514/6.1990-1697

[31] Hirschfelder, J. O., Curtiss, C. F., and Bird, R. B., *the Molecular Theory of Gases and Liquids*, Wiley, New York, 1954.

[32] Breck, D. W., *Zeolite Molecular Sieves: Structure, Chemistry, and use*, Wiley, New York, 1973, p. 636.

[33] Wilke, C. R., "A Viscosity Equation for Gas Mixtures," *Journal of Chemical Physics*, Vol. 18, No. 4, 1950, pp. 517–519. https://doi.org/10.1063/1.1747673

[34] Mortensen, C. H., "Effects of Thermochemical Nonequilibrium on Hypersonic Boundary-Layer Instability in the Presence of Surface Ablation or Isolated Two-Dimensional Roughness," Ph.D. Thesis, Univ. of California Los Angeles, California, 2015.

[35] Park, C., "On Convergence of Computation of Chemically Reacting Flows," AIAA Paper 1985-0247, 1985. https://doi.org/10.2514/6.1985-247

[36] Park, C., *Nonequilibrium Hypersonic Aerothermodynamics*, Wiley, New York, 1990.

[37] Bhutta, B. A., and Lewis, C. H., "Low-to-High Altitude Predictions of Three-Dimensional Ablative Re-Entry Flowfields," *Journal of Spacecraft and Rockets*, Vol. 30, No. 4, 1993, pp. 395–403. https://doi.org/10.2514/3.25544

[38] Johnston, C. O., "Influence of Coupled Radiation and Ablation on Meteor Entries," *47th AIAA Thermophysics Conference*, AIAA Paper 2017-4533, 2017. https://doi.org/10.2514/6.2017-4533

[39] Cohen, N., and Westberg, K. R., "Chemical Kinetic Data Sheets for High-Temperature Chemical Reactions," *Journal of Physical and Chemical Reference Data*, Vol. 12, No. 3, 1983, pp. 531–590. https://doi.org/10.1063/1.555692

[40] McBride, B., Heimel, S., Ehlers, J., and Gordon, S., "Thermodynamic Properties to 6000 K for 210 Substances Involving the First 18 Elements, NASA SP-3001, Office of Scientific and Technical Information," National Aeronautics and Space Administration, Lewis Research Center Cleveland, Ohio, 1963.

[41] Malcolm, W., and Chase, J., "NIST-JANAF Thermochemical Tables," *Journal of Physical and Chemical Reference Data*, Vol. 9, 1998, pp. 1–1856.

[42] Li, T., and Nagamatsu, H. T., "Hypersonic Viscous Flow on Non-insulated Flat Plate," TR ADA278404, Rensselaer Polytechnic Inst. Troy, New York, 1956.

[43] Nagamatsu, H. T., Pettit, W. T., and Sheer, R. E., Jr., "Heat Transfer On na Flat Plate In Continuum To Rarefied Hypersonic Flows at Mach Numbers of 19.2 and 25.4," No. DGLR PAPER 81-009, General Electric Research and Development Center, Schenectady, NY, 1970.

[44] Zhong, X., "High-Order Finite-Dierence Schemes for Numerical Simulation of Hypersonic Boundary-Layer Transition," *Journal of Computational Physics*, Vol. 144, No. 2, 1998, pp. 662–709. https://doi.org/10.1006/jcph.1998.6010

[45] Williamson, J., "Low-Storage Runge-Kutta Schemes," *Journal of Computational Physics*, Vol. 35, No. 1, 1980, pp. 48–56. https://doi.org/10.1016/0021-9991(80)90033-9

[46] Ma, Y., and Zhong, X., "Numerical Simulation of Receptivity and Stability of Nonequilibrium Reacting Hypersonic Boundary Layers," *AIAA 39th Aerospace Sconces Meeting and Exhibit*, AIAA Paper 2001-892, 2001. https://doi.org/10.2514/6.2001-892

[47] Celik, I. B., Ghia, U., Roache, P. J., Freitas, C. J., Coleman, H., and Raad, P. E., "Procedure for Estimation and Reporting of Uncertainty Due to Discretization in CFD Applications," *Journal of Fluids Engineering*, Vol. 130, No. 7, 2008, Paper 078001. https://doi.org/10.1115/1.2960953

[48] Narayan, N. M., Gopalkrishna, S. B., Mehdi, B., Ryll, S., Specht, E., and Fritsching, U., "Multiphase Numerical Modeling of Boiling Flow and Heat Transfer for Liquid Jet Quenching of a Moving Metal Plate," *International Journal of Thermal Sciences*, Vol. 194, 2023, Paper 108587. https://doi.org/10.1016/j.ijthermalsci.2023.108587

[49] Stephan, P., Kabelac, S., Kind, M., Mewes, D., Schaber, K., and Wetzel, T., *VDI Warmeatlas*, Springer-Verlag, Berlin, 2019.

D. Pytel
Associate Editor